doi:10.20944/preprints201811.0217.v1

Peer-reviewed version available at *Environments* **2018**, *5*, 129; doi:10.3390/environments5120129

Review

Understanding Land-Atmosphere-Climate Coupling from the Canadian Prairie dataset

Alan K. Betts [1,*] and Raymond L. Desjardins [2]

[1] Atmospheric Research, Pittsford, Vermont 05763, USA; akbetts@aol.com
[2] Agriculture and Agri-Food Canada, Ottawa, Ontario, Canada; ray.desjardins@canada.ca
* Correspondence: akbetts@aol.com; Tel.: +1-802-483-2087

Abstract: Analysis of the hourly Canadian Prairie data for the past 60 years has transformed our quantitative understanding of land-atmosphere-cloud coupling. The key reason is that trained observers made hourly estimates of opaque cloud fraction that obscures the sun, moon or stars, following the same protocol for 60 years at all stations. These 24 daily estimates of opaque cloud data are of sufficient quality that they can be calibrated against Baseline Surface Radiation Network data to give the climatology of the daily short-wave, longwave and total cloud forcing (SWCF, LWCF and CF). This key radiative forcing has not been available previously for climate datasets. Net cloud radiative forcing reverses sign from negative in the warm season to positive in the cold season, when reflective snow reduces the negative SWCF below the positive LWCF. This in turn leads to a large climate discontinuity with snow cover, with a systematic cooling of 10°C or more with snow cover. In addition, snow cover transforms the coupling between cloud cover and the diurnal range of temperature. In the warm season, maximum temperature increases with decreasing cloud, while minimum temperature barely changes; while in the cold season with snow cover, maximum temperature decreases with decreasing cloud and minimum temperature decreases even more. In the warm season, the diurnal ranges of temperature, relative humidity, equivalent potential temperature and the pressure height of the lifting condensation level are all tightly coupled to opaque cloud cover. Given over 600 station-years of hourly data, we are able to extract, perhaps for the first time, the coupling between cloud forcing and the warm season imbalance of the diurnal cycle; which changes monotonically from a warming and drying under clear skies to a cooling and moistening under cloudy skies with precipitation. Because we have the daily cloud radiative forci, which is large, we are able to show that the memory of water storage anomalies, from precipitation and the snowpack, goes back many months. The spring climatology shows the memory of snowfall back through the entire winter, and the memory in summer goes back to the months of snowmelt. Lagged precipitation anomalies modify the thermodynamic coupling of the diurnal cycle to the cloud forcing, and shift the diurnal cycle of mixing ratio which has a double peak. The seasonal extraction of the surface total water storage is a large damping of the interannual variability of precipitation anomalies in the growing season. The large land-use change from summer fallow to intensive cropping, which peaked in the early 1990s, has led to a coupled climate response that has cooled and moistened the growing season, lowering cloud-base, increasing equivalent potential temperature, and increasing precipitation. We show a simplified energy balance of the Prairies during the growing season and its dependence on reflective cloud.

Keywords: Climate; land-atmosphere interaction; clouds; diurnal cycle; snow cover; Prairies; land-use; hydrometeorology.

1. Introduction

Understanding land-atmosphere-climate coupling is challenging because so many coupled processes are involved: soil temperature and moisture, vegetation types, properties and coverage; near-surface temperature and humidity; the atmospheric boundary layer; the shallow and deep cloud fields which determine the surface radiation balance and surface precipitation, the soil hydraulic properties that determine the surface and deep runoff, to name only local components. In the cold season precipitation falls as snow and the surface accumulation increases the albedo, and stores water till snowpack melt.

The coupling between the energy and water cycles at the land-surface is central to hydrometeorology and important to weather forecasts on timescales from days to seasons. Earlier reviews [1,2] looked at hydrometeorology from the global modeling perspective using model reanalysis data, which showed how net longwave and shortwave radiation, cloud cover, surface fluxes, diurnal temperature range, soil moisture and cloud-base height were coupled on daily timescales over river basins [3]. On daily timescales, the land-atmosphere system is fully coupled, so errors in the model representation of processes in the soil, vegetation, boundary layer and cloud fields can rapidly bias a model forecast. Nonetheless, this model perspective was a strong motivation for our analyses of the Canadian Prairie data, and the search for a quantitative description of the fully coupled observed system.

Historically many climate and hydrometeorology studies have been largely based on precipitation, temperature and humidity for which long-term records are available [4-6]. However the diurnal cycle is driven primarily by the surface radiation balance, which depends critically on the daily cloud fields, which are generally unknown in climate records, until satellite-based estimates became available. We cannot study the fully coupled nature of the land-atmosphere-climate system without the surface radiation budget.

The Canadian Prairie data, which is the focus of this review, is however an exception, because observers, typically at most major airports, were trained to estimate hourly the opaque cloud fraction in tenths by cloud level and in total. The definition of opaque cloud is “opaque to the sun, moon or stars”; and this protocol has been followed by trained observers hourly for 60 years across the Prairies. With 24 observations per day (almost none are missing), we have representative estimates of the fraction of the daytime shortwave clear-sky (SWCS) flux reaching the surface and the fraction of the sky that is opaque to outgoing longwave (LW) radiation for over 600 station-years of data. Because there are 17 years of Baseline Surface Radiation Network (BSRN) data just 25 km south of Regina, SK, we were able to calibrate the opaque cloud data in terms of the LW and SW cloud forcing (section 3.3). This is transformative as it meant we were able to determine quantitatively the climate coupling between the cloud radiative forcing and the diurnal and seasonal cycle. In addition, simply because we can separate the large radiative impact of clouds from the impact of precipitation, we can better quantify the hydrometeorological processes that couple the energy and water cycle, and observe the long-term memory of precipitation anomalies. In recent years, data from the Gravity Recovery and Climate Experiment (GRACE) [7,8] give estimates of the seasonal drawdown of total water storage. Canadian archives also record agricultural crops grown on the Prairies back to 1955, so we could assess the large climate impact of the shift away from summer fallowing to continuous cropping.

This review will outline our key conclusions from a series of papers [9-16]. Readers interested in more details, or in the evolution of our thinking can refer back to these original papers. It is remarkable that the long-term Prairie climate dataset, with better cloud observations, have taken our understanding of land-atmosphere-climate coupling to a new level. In retrospect, much of our analysis could have been done two decades ago, but the data was not widely accessible.

Section 2 discusses the Prairie data and our analysis. Section 3 outlines how the climate is coupled to opaque cloud and snow cover on daily timescales, and shows the difference in cloud forcing between warm and cold season with snow. Section 4 looks at the long-term memory of precipitation anomalies, both using multiple regression for the cold and warm seasons, and the dependence of the diurnal coupling on opaque cloud and precipitation anomalies. Section 5 looks at

Peer-reviewed version available at *Environments* **2018**, *5*, 129; doi:10.3390/environments5120129

how the seasonal extraction of the surface total water storage damps the interannual variability of precipitation anomalies in the growing season; and how the large land-use change from summer fallowing to intensive cropping has led to a coupled climate response. Finally we return to reanalysis data to show how the growing season surface and top-of-atmosphere (TOA) budgets change with cloud cover. Section 6 summarises our conclusions.

2. Processing the Prairie dataset

2.1 Station Locations

Figure 1 shows the location of the 15 Prairie stations used in our analyses. Most of the stations are in the agricultural region. Table 1 lists the station locations and elevation and the two letter code we will use to identify stations in figures and text. These Prairie data have a full hourly set of pressure, temperature, relative humidity, wind speed and direction, opaque cloud and derived radiation, as well as daily precipitation and snow depth. The hours of missing data is remarkably small. For key stations, such as Calgary, Regina and Winnipeg, more than 99.9% of the days have no missing hours in the first 40 years. In more recent years since 1994, the number of days with less than 23 hours of data is typically less than 1%. A few stations (PS in 1992; MJ in 1998; LE and MH in 2006) shifted to daytime-only observation in recent years, because of reduced staffing.

Since opaque cloud reflects the solar flux and traps the outgoing longwave, our initial focus was to use the daily mean of the hourly opaque cloud measurements to stratify the daily mean data and the diurnal ranges of temperature and humidity and derived variables (see section 3).

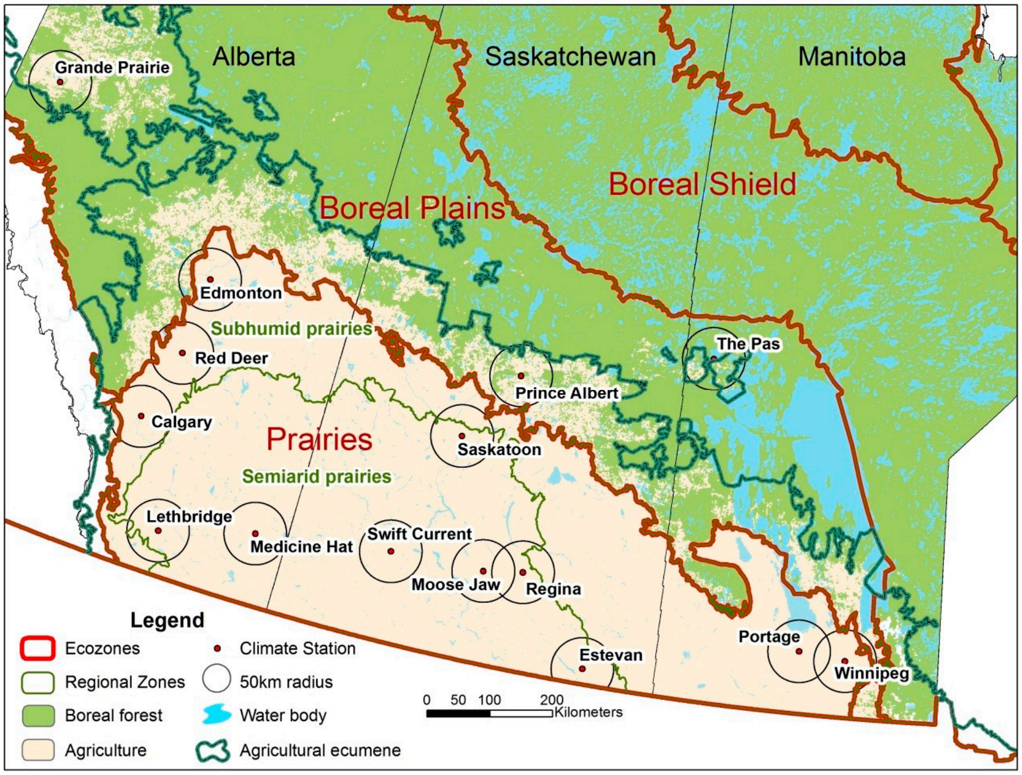

Figure 1. Climate station locations, Canadian ecozones, regional zones, agricultural regions and boreal forest.

Peer-reviewed version available at Environments 2018, 5, 129; doi:10.3390/environments5120129

Table 1. Climate stations with locations and elevation.

Station Name (Code)		Station ID	Province	Latitude	Longitude	Elevation (m)
Red Deer	(RD)	3025480	Alberta	52.18	-113.62	905
Calgary	(CA)	3031093	Alberta	51.11	-114.02	1084
Edmonton	(ED)	3012202	Alberta	53.57	-113.52	671
Lethbridge	(LE)	3033880	Alberta	49.63	-112.80	929
Medicine Hat	(MH)	3034480	Alberta	50.02	-110.72	717
Grande Prairie	(GP)	3072920	Alberta	55.18	-118.89	669
Regina	(RG)	4016560	Saskatchewan	50.43	-104.67	578
Moose Jaw	(MJ)	4015320	Saskatchewan	50.33	-105.55	577
Estevan	(ES)	4012400	Saskatchewan	49.22	-102.97	581
Swift Current	(SW)	4028040	Saskatchewan	50.3	-107.68	817
Prince Albert	(PA)	4056240	Saskatchewan	53.22	-105.67	428
Saskatoon	(SK)	4057120	Saskatchewan	52.17	-106.72	504
Portage-Southport	(PS)	5012320	Manitoba	49.9	-98.27	270
Winnipeg	(WI)	5023222	Manitoba	49.82	-97.23	239
The Pas	(TP)	5052880	Manitoba	53.97	-101.1	270

2.2 Diurnal range definition

The diurnal range of temperature, DTR, is defined as the difference between the maximum temperature, T_x, and the minimum temperature, T_n

$$DTR = T_x - T_n \tag{1a}$$

Similarly for relative humidity, RH, (and other variables), we define the diurnal range, DRH, as the difference between the maximum, RH_x, and the minimum, RH_n

$$DRH = RH_x - RH_n \tag{1b}$$

In our early papers [9-13] we generally reduced the hourly data to daily means, T_m, RH_m, and recorded T_x, T_n, and DTR. The difference in relative humidity, RH, between T_n and T_x was used as an approximation of the diurnal range DRH. However, there has been considerable discussion in recent years about the difference between DTR, T_x and T_n derived from monthly means of hourly data, and the conventional monthly mean of daily values of DTR, T_x and T_n [12,17-19].

We explored this issue [14], using stratifications by month and by opaque cloud cover, and found systematic biases especially in winter, and even in summer under cloudy conditions. We concluded that the radiatively-forced diurnal cycle, that is the lagged response to the diurnally varying radiation field, which is dependent on opaque cloud cover, is represented best by first binning the hourly data for groups of many days, and then determining the diurnal ranges from the composites. Specifically we found that this radiatively-forced diurnal cycle has a smaller amplitude than the corresponding average of the daily ranges. The reason is transparent. Without advection of temperature, T_n is near sunrise and T_x is in the mid-afternoon, but advection can shift the daily minimum temperature away from the time of sunrise to a lower value than the temperature at sunrise, and similarly advection can shift the daily maximum temperature away from the mid-afternoon to a higher value than the mid-afternoon temperature. Either will give a larger diurnal range.

Our dataset has around 240,000 days, so coarse stratifications may have 2000 days in each bin, and detailed sub-stratifications typically have >200 days in each bin. This means that the radiatively-forced diurnal cycle emerges from composites of the hourly data, since advection of temperature and humidity varies from day to day. This leads to a fundamental quantitative improvement in our

Peer-reviewed version available at *Environments* **2018**, *5*, 129; doi:10.3390/environments5120129

understanding of the coupling between the diurnal cycle and opaque cloud cover that determines the cloud radiative forcing.

We also derived from T, RH and surface pressure, PS, the other thermodynamic variables: the mixing ratio (Q), the potential temperature (θ), the equivalent potential temperature (θ_E) and the saturation pressure (p*) at the lifting condensation level (LCL). We defined the pressure height to the LCL, $P_{LCL} = PS - p^*$ [2], which in the warm season is often an indicator of the height of cloud base [9]. We calculated the diurnal ranges that are related to moist convective processes

$$D\theta_E = \theta_{Ex} - \theta_{En} \tag{2a}$$

$$DP_{LCL} = P_{LCLx} - P_{LCLn} \tag{2b}$$

2.3 Opaque cloud bins

We computed two daily averages from the all-sky opaque cloud cover estimates to use for stratification. The first is the simple mean of the 24 hourly values, $OPAQ_m$. The second, OPAQSW, is a mean of the hourly opaque cloud values during daylight hours, weighted by a fit to the downward clear sky flux derived from the reanalysis know as ERA-Interim (details in [13]).

3. Climate Coupling to opaque cloud and snow cover

This section will present several topics: cloud forcing of the diurnal cycle, the differences in cloud forcing between the warm season and the cold season with snow cover, the relationship between opaque cloud and cloud radiative forcing, the climate impact of snow cover, the coupling between opaque cloud and warm season diurnal ranges and the dependence of the 24-h imbalances of the diurnal cycle on opaque cloud cover.

3.1 Cloud forcing of diurnal cycle

We start by summarizing the important results from [14]. Figure 2 shows the composite of the mean diurnal cycle of temperature, stratified by month and ten bins of daily mean opaque cloud, $OPAQ_m$, and partitioned into a warm group of days with T_m>0°C and no snow cover (141160 days), and a cold group of days with T_m<0°C with surface snow cover (74260 days).

Figure 2 uses a different color scheme for the composites with and without snow. In the warm season from May to September, we see a steep increase of maximum temperature T_x and diurnal temperature range DTR with decreasing opaque cloud, and a rather small fall of minimum temperature in summer. In sharp contrast, in the cold season with snow, December to February, T_x decreases with decreasing opaque cloud and T_n decreases even more steeply to its lowest minimum at sunrise under clear skies. For the transition months, November, March and April between warm and cold seasons, we see both stratifications; and it is apparent that the distributions with and without snow are non-overlapping. Specifically, snow cover cools the mean climate, represented by mean temperature, T_m, by about 10°C, and this cooling increases under clear skies (see section 3.4 later). Snow cover acts as a climate switch between these two non-overlapping regimes.

This is a large dataset with about 20000 days per month, so that each cloud bin has typically about 2000 days in summer and winter. For the transition months, where the data is also split unevenly, we only show the diurnal cycle where the number in each cloud bin exceed 150 days.

Peer-reviewed version available at *Environments* **2018**, *5*, 129; doi:10.3390/environments5120129

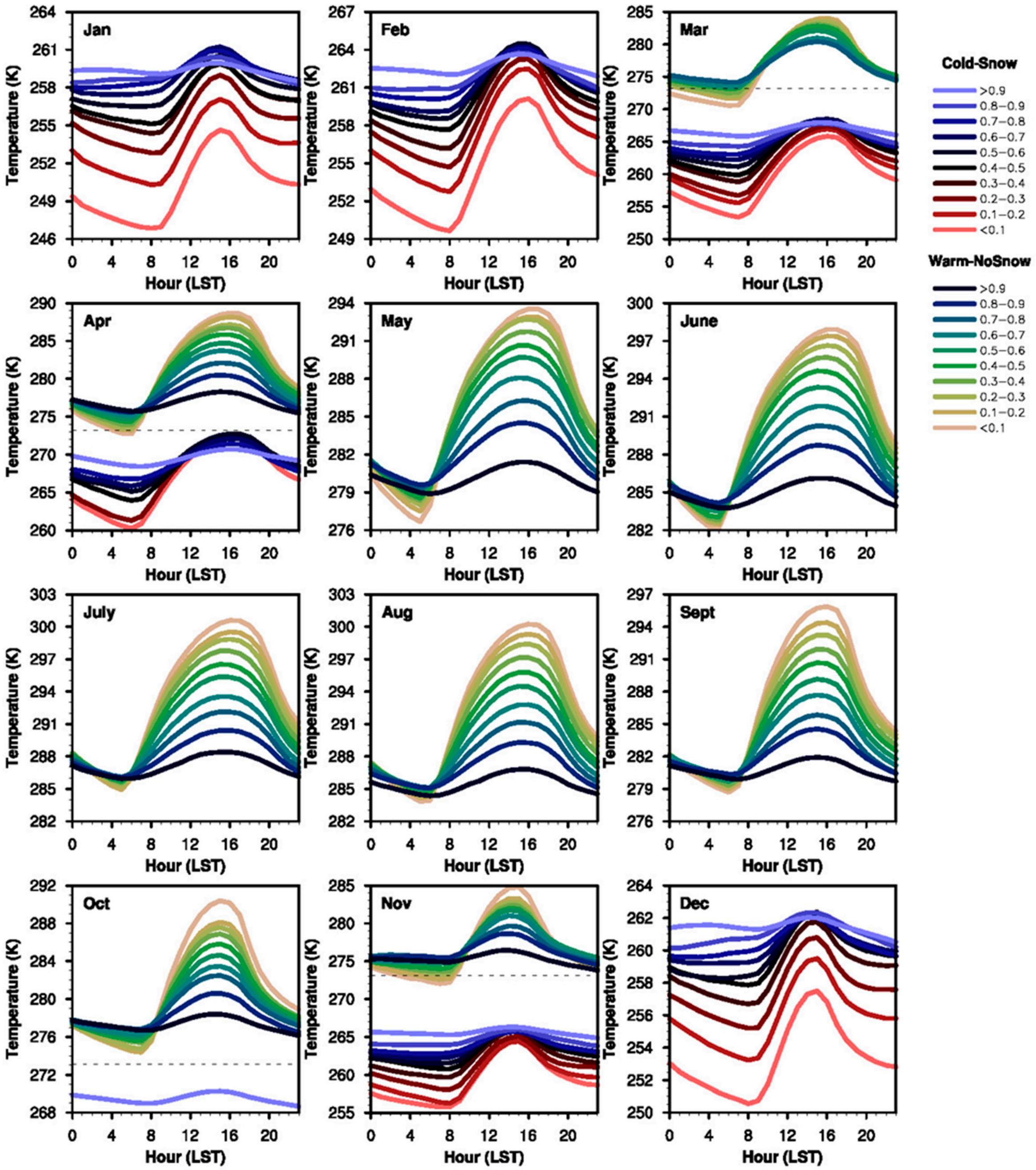

Figure 2. Monthly diurnal cycles for cold-snow and warm-no-snow classes, stratified by opaque cloud.

3.2 Change of cloud forcing between warn and cold season

The dramatic differences in the diurnal cycles of temperature shown in Figure 2 are related to the reversal of the sign of the net cloud forcing between warm season and cold season with snow cover. This we computed using data from the Baseline Surface Radiation Network (BSRN) Prairie site at Bratt's Lake, Saskatchewan at 50.204°N, 104.713°W, elevation 588 m [13]. We have 17 years of the downwelling fluxes, SW_{dn} and LW_{dn}, at Bratt's Lake, which we first averaged from 1-min data to hourly means, and then to daily means.

In the shortwave radiation budget, we can define an effective cloud albedo (ECA) and the shortwave cloud forcing (SWCF) in terms of a downwelling SW clear-sky flux, $SWCS_{dn}$, based on a fit to the clear-sky fluxes from the nearest grid-point of the reanalysis ERA-Interim [20, 13]

Peer-reviewed version available at Environments 2018, 5, 129; doi:10.3390/environments5120129

$$ECA = 1 - SW_{dn} / SWCS_{dn} \tag{3}$$

$$SWCF = SWCS_{dn} - SW_{dn} \quad = - ECA*SWCS_{dn} \tag{4}$$

The dimensionless ECA, with a range from 0 to 1, is a useful measures of the impact of the reflective cloud field on the surface shortwave radiation budget [2, 3]. SWCF becomes increasingly negative as ECA increases, while $SWCS_{dn}$ has a large increase from the winter to the summer solstice.

Similarly we can define a longwave cloud forcing (LWCF) in terms of a downwelling clear-sky flux $LWCS_{dn}$ also from ERA-Interim as

$$LWCF = LW_{dn} - LWCS_{dn} \tag{5}$$

$LWCS_{dn}$ is the smaller term, and LW_{dn} increases with increasing cloud cover, so LWCF is positive.

The total cloud forcing (CF) of the downwelling radiative fluxes is the sum

$$CF = SWCF + LWCF \tag{6a}$$

In the warm season, the SWCF dominates and CF is negative. The net cloud forcing can be defined as

$$CF_{net} = (1 - \alpha_s)\, SWCF + LWCF \tag{6b}$$

where the mean surface albedo, defined as

$$\alpha_s = SW_{dn}/SW_{up} \tag{7}$$

ranges for Saskatchewan from about 0.18 in summer to 0.73 in winter with snow cover [3,4]. When there is a snow cover, the positive LWCF dominates, because the lower solar elevation and larger surface albedo greatly reduce the net SWCF. Figure 3 shows that CF_{net} reverses sign from increasing negative with cloud cover in the warm season, to increasing positive in the cold season with cloud cover. This is consistent with the daily mean temperature response seen in Figure 2 to changing opaque cloud cover.

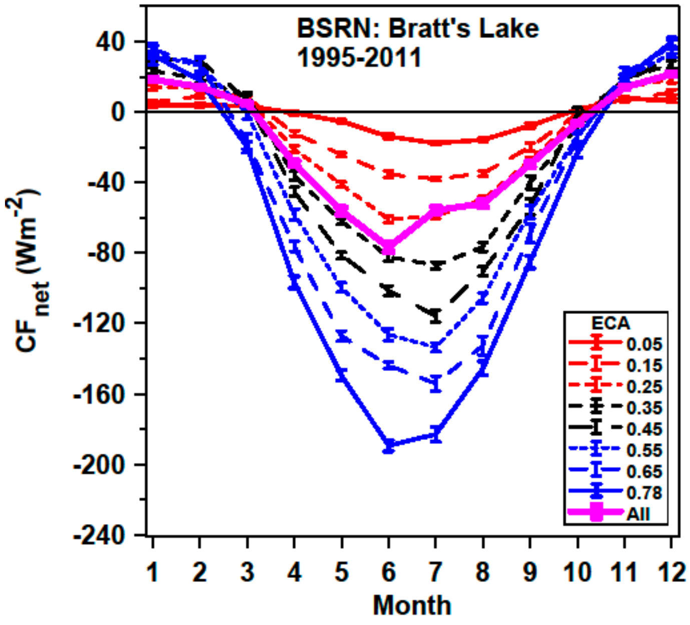

Figure 3. Mean annual cycle of CF_{net} stratified by ECA.

3.3 Relationship between opaque cloud and cloud radiative forcing

We then binned the BSRN data from Bratt's Lake for the downward SW and LW fluxes using the opaque cloud measurements at Regina, 25 km to the north, separating warm and cold season

Peer-reviewed version available at *Environments* **2018**, *5*, 129; doi:10.3390/environments5120129

simply by daily mean T_m > < 0°C, since we have no snow cover data for Bratt's Lake. For the SW comparison, we compared the daytime weighted opaque cloud, OPAQSW (see section 2.3) with ECA from equation (3). For the LW comparison, we compared the 24h mean $OPAQ_m$ with the net LW flux

$$LW_n = LW_{dn} - LW_{up} \tag{8}$$

We calculated an estimate of LW_{up} from the daily mean air temperature, T_m (°C), using T_k (K) = T_m+273.15, from

$$LW_{up} = \varepsilon\ \sigma\ T_k^4 \tag{9}$$

with $\sigma = 5.67\text{x}10^{-8}$ (W m^{-2} K^{-4}) and the emissivity ε set to 1.

Figure 4 (left) shows the relationship between ECA and OPAQSW for the warm season above freezing and the cold season below freezing. ECA increases more steeply with increasing opaque cloud in the warm season than the cold season. We show the mean and standard error of the binned data, and the quadratic regression fits to the daily data. For the warm season, the fit is ($R^2 = 0.87$)

$$ECA = 0.06(\pm0.08) + 0.02(\pm0.02)\ OPAQSW + 0.65(\pm0.02)\ OPAQSW^2 \tag{10a}$$

For the cold season, the fit is ($R^2 = 0.71$)

$$ECA = 0.07(\pm0.11) + 0.08(\pm0.03)\ OPAQSW + 0.37(\pm0.03)\ OPAQSW^2 \tag{10b}$$

The uncertainty in ECA on a daily basis is of the order of ±0.08 in the warm season and ±0.11 in the cold season. The standard errors (SE) shown for the climatological fits are much smaller because they are reduced by the large number of days.

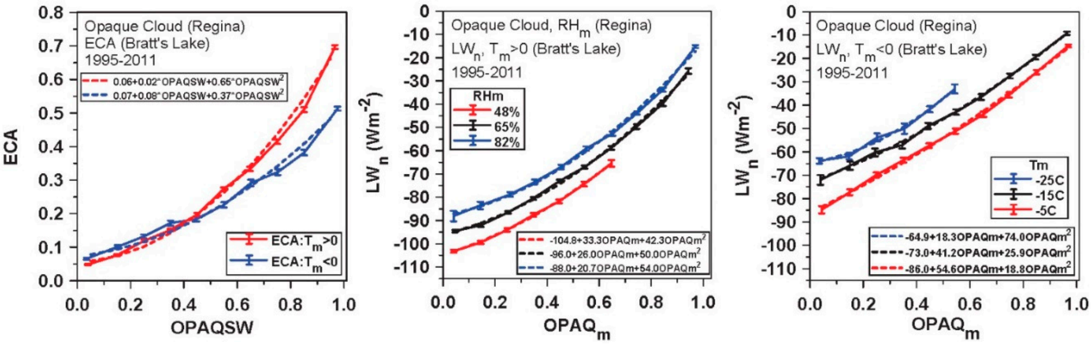

Figure 4. Relationship between opaque cloud at Regina and Bratt's Lake ECA (left), opaque cloud and LW_n stratified by RH_m in warm season (middle) and (right) LW_n stratified by T_m in cold season.

Figure 4 (middle) shows the dependence of LW_n on opaque cloud and daily mean RH_m (taken from Regina because RH was not measured at Bratt's Lake for the first 5 years) for days above freezing (3245 days). Increasing atmospheric humidity reduces the outgoing LW_n flux for the same cloud cover. The temperature dependence is very small when T_m>0°C (not shown). In contrast for temperatures below freezing (2198 days), the humidity dependence is small but the temperature dependence is significant, as shown in the right panel. The outgoing LW_n flux now decreases with colder temperatures, probably because the surface cools under a stable BL in the cold season [12].

The quadratic fits in the two right panels are the fits to the binned data. In the warm season, multiple regression of the daily values of LW_n on quadratic opaque cloud and RH_m gives ($R^2 = 0.91$)

$$LW_n = -128.6(\pm7.8) + 28.1(\pm1.8)OPAQ_m + 44.6(\pm1.8)OPAQ_m{}^2 + 0.49(\pm0.01)RH_m \tag{11a}$$

In the cold season, multiple regression on quadratic opaque cloud, T_m and RH_m gives ($R^2 = 0.83$)

$$LW_n = -112.2(\pm9.8) + 43.5(\pm2.8)OPAQ_m + 26.8(\pm2.5)OPAQ_m{}^2 + 0.29(\pm0.02)RH_m - 1.02(\pm0.03)T_m \tag{11b}$$

3.4 Climate impact of snow cover

Peer-reviewed version available at Environments 2018, 5, 129; doi:10.3390/environments5120129

Figure 2 shows that the climate impact of snow cover on the Prairies on the diurnal cycle of temperature is very large. The transition months show a large cooling with snow cover and a reversal of the response to cloud cover, consistent with the reversal of the net cloud forcing between cold and warm seasons shown in Figure 3.

Figure 5 shows four different analyses of the impact of snow cover. Top-left is a composite of the six stations in Saskatchewan for 8 days before and after fresh snowfall in November, showing a mean of about 270 snowfall events with a mean date of November 15 (adapted from [11]). We see the fall of daily mean temperature across the snow event, from near 0°C a week before to -9.4 ± 0.7°C for days 2 to 8 afterwards. The albedo of the Prairies changes from about 0.2 with no snow cover to above 0.7 with snow cover [3,4], and this is linked to a nearly 10°C fall of temperature. The climate transition from fall to winter often comes abruptly with these snow events [11], as the snowpack may not melt till spring.

Top-right (adapted from [14]) shows the fall of mean daily temperature, δT_m, with snow cover; derived from Figure 2 by differencing the diurnal composites with and without snow for November and March for each opaque cloud cover bin. We made a correction of about 2°C, based on the mean seasonal cycle [14] to allow for the fact that the mean date of the snow-free composite is about 15 days earlier in November and later in March than the composite with snow. The curves are a little noisy, because the independent sampling in opaque cloud bins, with and without snow, is far from homogeneous; and in these transition months, the number of days in each bin ranges widely from 184 to 1869 (not shown). Nonetheless, we see larger cooling as opaque cloud decreases. The climate cooling with snow, averaged across all cloud bins (open circles), is -11.8°C (-10.7°C) for November (March). We also show quadratic fits (dashed) as a useful smooth reference for the impact of cloud cover. We note that the radiative forcing is stronger in March than November, but we cannot assess whether the small difference between the November and March curves is significant, given the inhomogeneity across cloud bins.

The bottom-left plot shows the mean monthly temperature across the cold season (black line) and the partition into days with snow cover (blue) and days with no snow cover (red line) for a single station (Lethbridge, Alberta); together with the mean snow depth. The difference between the blue and red curves (the magenta curve) shows the monthly climate cooling of snow cover with a mean value of $\Delta T = -10.4 \pm 0.4$°C. The standard errors shown are small because of the large number of days in the 49-year record. Other stations show similar plots, suggesting that the cold season climatologies with and without snow (red and blue curves) are quite distinct and non-overlapping. Conventionally, they are merged to the black curve, so this can be misleading.

The bottom-right panel shows the mean temperature T_M, for October to April against the fraction of days with snow cover (FDS) for five stations in Alberta, Lethbridge, Medicine Hat, Calgary, Red Deer and Grande Prairie, listed in order of increasing latitude (adapted from [12,15]). The line fit shown is for 326 years of data, and we show the station means (black circles), which lie close to this line fit. Since it is clear that the southern three stations (red points) have warmer temperatures and lower FDS than the northern two stations, we also computed the linear regression slopes for these two groups.

All station fit $$T_M = 3.9(\pm 1.2) - 14.6(\pm 0.5)*FDS \qquad (R^2=0.79) \qquad (12a)$$

3 southern station fit $$T_M = 3.8(\pm 1.5) - 14.3(\pm 0.7)*FDS \qquad (R^2=0.73) \qquad (12b)$$

2 northern station fit $$T_M = 3.2(\pm 1.5) - 13.6(\pm 1.5)*FDS \qquad (R^2=0.48) \qquad (12c)$$

These agree within the uncertainty, which increases for fewer stations. We conclude that the climate coupling between fraction of days with snow cover and mean cool season temperature is a robust feature of the Prairie landscape. The shift of the station means with increasing latitude suggests reduced insolation is also playing a tightly coupled role.

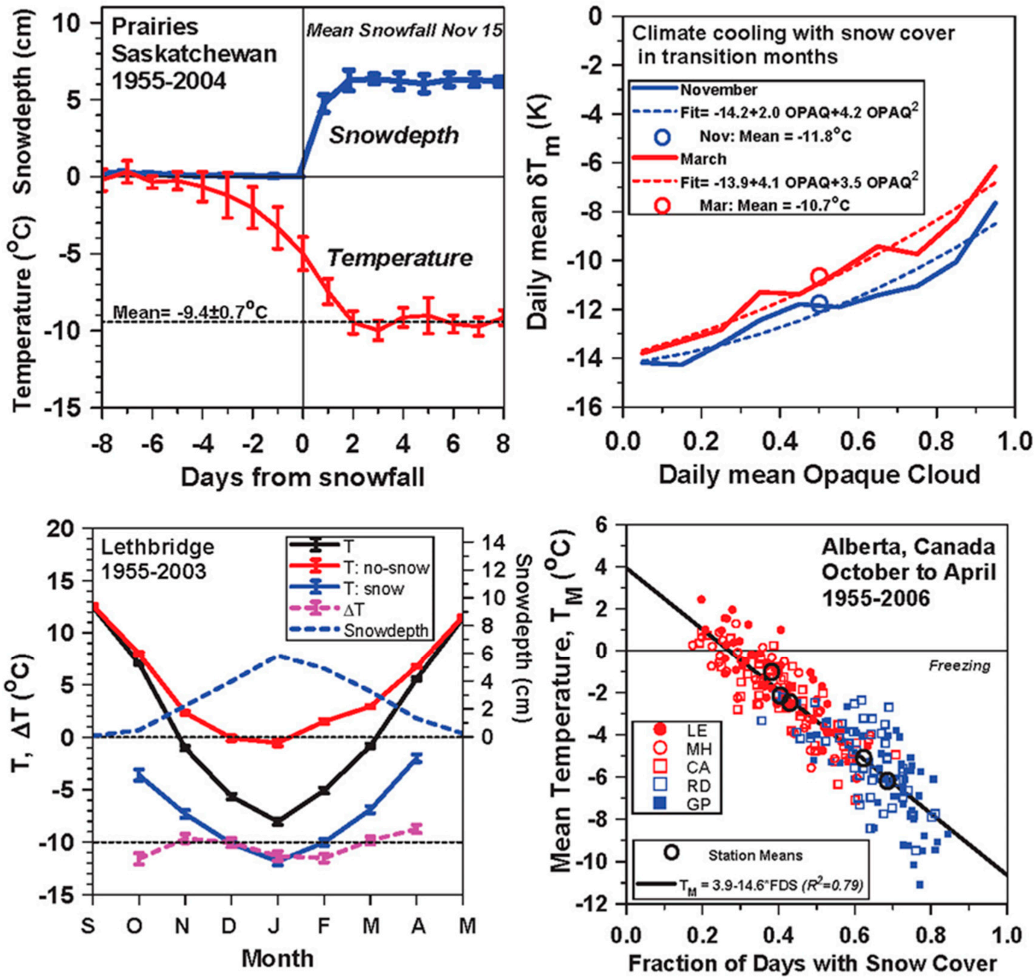

Figure 5. Drop of temperature with fresh snowfall (top-left), climate cooling with snow cover in November and March as a function of opaque cloud (top-right), 10°C separation of cold season climates with and without snow cover (bottom-left), and (bottom-right) dependence of mean cold season temperature on fraction of days with snow cover.

Figure 5 confirms that snow cover has a large cooling impact on mean temperatures in the cold season: that is snow cover acts as a climate switch between two non-overlapping regimes. On daily timescales, the cooling is about -10°C for the Prairies, where the surface albedo with snow cover is of order 0.7. The larger slope of -14.6°C in fit (12a) for the change of mean cold season temperature with the fraction of days with snow cover suggests that there may be coupling to larger scales that enhance the regional cooling with snow cover.

3.5 Coupling of warm season diurnal ranges and 24-h imbalances to opaque cloud

This very large hourly dataset allowed us for the first time to extract the radiatively forced diurnal ranges [14] for the key thermodynamic variables shown in equations (1) and (2) for both cold and warm seasons. Here we will just show the warm season. DTR comes from Figure 2 as a function of opaque cloud and month, while DRH, $D\theta_E$, DP_{LCL} come from similar diurnal composites (not shown). Further examination of Figure 2 shows that there is discontinuity across local midnight that also depends on opaque cloud cover. So we calculated, also for the first time, this 24h imbalance of the diurnal cycle as a function of opaque cloud and month. These are key conceptual improvements in our quantitative understanding of the diurnal cycle over land in the warm season.

Figure 6 (top left panel) shows the mean diurnal ranges of temperature, DTR, relative humidity, DRH, and mean daily precipitation for the warm season months April to September with no snow. Remarkably, the diurnal ranges are tightly clustered [9, 14], so we also show the 6-month warm season mean. The quadratic regression fits for the dependence of the 6-month mean DTR and DRH on $OPAQ_m$ are

$$DTR = 16.7(\pm 0.4) - 9.3(\pm 0.8)*OPAQ_m - 6.0(\pm 0.7)*OPAQ_m^2 \quad (R^2=0.992) \tag{13a}$$

$$DRH = 47.5(\pm 0.8) - 2.6(\pm 1.4)*OPAQ_m - 38.9(\pm 1.4)*OPAQ_m^2 \quad (R^2=0.996) \tag{13b}$$

The leading coefficient is the clear-sky diurnal range, which is a rise of 16.7°C to the afternoon maximum, coupled to a fall of 47.5% in RH from the morning maximum at sunrise. The cloudy limit for $OPAQ_m$ =1, given by these fits, are the small values (DTR, DRH) = (1.4°C , 6.0%).

Monthly mean precipitation is very low for $OPAQ_m < 0.4$, and the increase of precipitation with $OPAQ_m$ is largest in summer, peaking in July when T and mixing ratio Q also peak. However, because June has substantially greater opaque cloud cover [12], mean June precipitation (2.28 mm d^{-1}) is greater than July (1.91 mm d^{-1}).

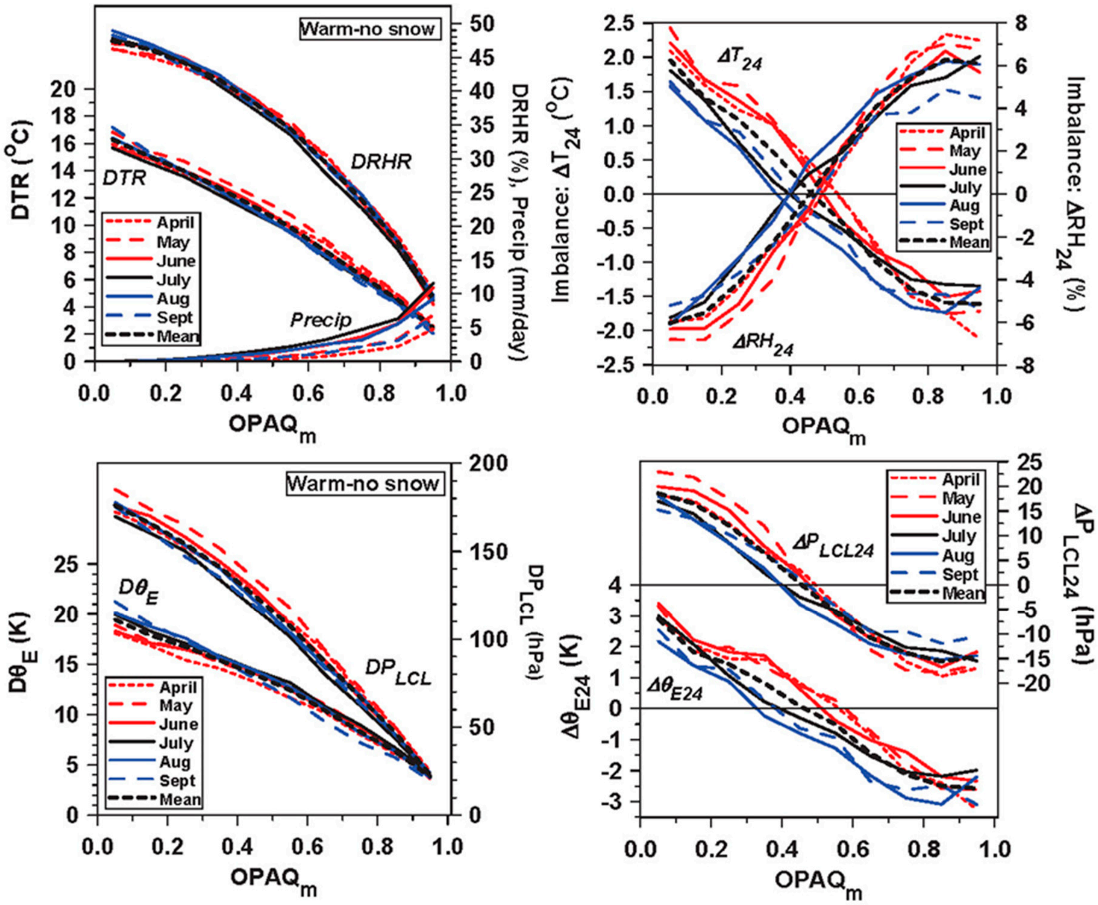

Figure 6. The opaque cloud dependence of the diurnal ranges of T, RH, θ_E and P_{LCL} (left) and (right) the 24h imbalance of the diurnal cycle.

Figure 6 (top right) shows the 24-h imbalances of ΔT_{24} and ΔRH_{24}, which we calculated from the discontinuities across local midnight [14]. We see that as $OPAQ_m$ changes from 0.05 to 0.95, the mean (ΔT_{24}, ΔRH_{24}) change monotonically from (+2°C, -6%) to (-1.5°C, +6%). Under nearly clear skies, the warming and drying over the diurnal cycle is slightly larger in April, May and June as seasonally the mean temperature is increasing, and slightly smaller in August and September. Note however that we see a larger increase in ΔRH_{24} in April and May under cloudy skies. The SE of the hourly binned data from which Figure 6 is derived is ≈0.1K for T, ≤0.5% for RH.

Thus we see under nearly clear skies, a warming of +2°C and a drying of -6% over the diurnal cycle, which is about 12% of both DTR and DRH. At the other limit under very cloudy skies, typically with rain, the cooling of -1.5°C and moistening of +6% may be partly driven by both the evaporation of rain and downdraft transports. Between these limits, there is a uniform progression with increasing cloud, and for the 6-month mean, ΔT_{24} and ΔRH_{24} cross zero for $OPAQ_m = 0.45$. So a steady state diurnal cycle only exists under partly cloudy conditions. This presents a conceptual challenge to equilibrium models for the non-precipitating convective BL over land [21].

Figure 6, lower panels, show the corresponding warm season diurnal ranges and 24-h imbalances for θ_E and P_{LCL}. Again the diurnal ranges and the diurnal imbalances have only a small spread from April to September. The quadratic fits for the $OPAQ_m$ dependence of the 6-month means are

$$D\theta_E = 19.7(\pm0.7) - 9.4(\pm1.2)*OPAQ_m - 7.5(\pm1.2)*OPAQ_m^2 \qquad (R^2=0.983) \qquad (14a)$$

$$DP_{LCL} = 181.4(\pm4.9) - 90.3(\pm9.0)*OPAQ_m - 81.1(\pm8.7)*OPAQ_m^2 \qquad (R^2=0.991) \qquad (14b)$$

Again the leading coefficient is the clear-sky diurnal range, which is a rise of (θ_E, P_{LCL}) = (19.7K, 181.4hPa) from the morning sunrise minimums. The cloudy limit for $OPAQ_m$ =1, given by these fits, are the small values ($D\theta_E$, DP_{LCL}) = (2.73K, 10.0hPa).

The bottom-right panel for the corresponding monthly mean 24-h imbalances shows that under nearly-clear skies, there is an increase of +2.9K for $\Delta\theta_{E24}$ and +18.6hPa for ΔP_{LCL24}, which are 14.9% and 10.5% of the respective diurnal ranges. There is a corresponding small 24-h imbalance of mixing ratio, ΔQ_{24}, of +0.2 gkg^{-1} (not shown). At the other limit under nearly-overcast skies, typically with rain, the 24-h imbalance is a fall of -2.6K for $\Delta\theta_{E24}$ and -14.6 hPa for ΔP_{LCL24}, with a corresponding fall of ΔQ_{24} of -0.24 gkg^{-1} (not shown). The SE of the hourly binned data from which these plots are derived is ≤0.3K for θ_E and ≤1.5hPa for P_{LCL}. On the seasonal timescale, we see that the imbalance of $\Delta\theta_{E24}$ is larger in April, May and June over most of the $OPAQ_m$ range as the climate warms, and smaller in August and September. However for ΔP_{LCL24} the seasonal response has an asymmetric structure consistent with ΔRH_{24}, since lower RH is tightly coupled to higher P_{LCL}.

Figure 6 shows the remarkably tight climatological coupling from April to September which links opaque cloud cover, the diurnal ranges and the 24h diurnal imbalances, despite substantial differences in the solar zenith angle. Over the diurnal cycle, under nearly clear skies, we see a warming and drying, and a rise of θ_E and P_{LCL}. At the cloudy extreme with rain, we see 24h imbalances of opposite sign that are generally slightly smaller. These rather precise warm season patterns across opaque cloud cover, and therefore cloud radiative forcing, set a clear target for modeling the partially cloudy boundary layer over land.

4. Hydrometeorology memory on monthly timescales

The close coupling between the energy and water cycles at the land-surface is central to hydrometeorology and important to weather forecasts on timescales from days to seasons. An earlier review looked at hydrometeorology using global model reanalysis data [1], which showed how net longwave and shortwave radiation, cloud cover, surface fluxes, diurnal temperature range, soil moisture and cloud-base height were coupled on daily timescales over river basins. Reanalysis data contain all the key variables, but historically the observed near-surface climate variables were temperature and precipitation, along with pressure, wind, relative humidity and snow-depth. Section 3.5 shows that the warm season diurnal cycle is dominated by the radiative forcing of the opaque cloud cover. But on monthly and longer timescales, soil moisture anomalies are linked to precipitation anomalies, both for the current month and several preceding months.

Here we summarize some key results from [16], who merged the 12 stations in Table 1 in Alberta and Saskatchewan for the period when precipitation and snow data are available, which was typically 1955-2006. For this monthly analysis, the hourly data were processed as intact monthly mean diurnal cycles for each station for each year. As noted in section 2.1, the hourly dataset is remarkably complete. Days were omitted if <20 hours of data were available. Months were omitted if they had fewer than 28 days remaining, except for February where this threshold was reduced to 25 days. From the monthly diurnal cycles of T, RH, PS, we computed the derived thermodynamic variables, Q, θ_E, P_{LCL} and the diurnal ranges defined in equations (1) and (2).

For each variable, Y, we extracted from the monthly mean diurnal cycles, the daily mean, Y_m, the maximum and minimum, Y_x and Y_n, and the times of the maximum and minimum [14]. We then computed the long-term station monthly mean, and used these to compute monthly anomalies, δY. For the daily precipitation and snow-depth, we also computed monthly means, the long-term station monthly means, and used these to compute monthly anomalies for each station. The monthly anomalies of opaque cloud, precipitation, snow-depth and snow cover frequency were then standardized by their monthly standard deviation (SD). For the temperature anomalies, δT_m, δT_x, δT_n, and the diurnal temperature range, δDTR, we standardized by the monthly SD of δT_m. Similarly for the variables, δRH_m, δRH_x, δRH_n and the diurnal RH range δDRH, we standardized by the monthly SD of δRH_m. The corresponding set of anomalies for equivalent potential temperature, $\delta\theta_E$, and pressure-height to the LCL, δP_{LCL}, were standardized by the monthly SD of $\delta\theta_{Em}$, and δP_{LCLm} respectively.

We used multiple linear regression to explore the correlation between variables. Following [12,16], our starting format was to regress a standardized thermodynamic anomaly, δY, on opaque cloud anomalies ($\delta OPAQ_m$) for the current month, and lagged precipitation anomalies for the current month (δPR0) and preceding months (δPR1, δPR2, δPR3, δPR4, δPR5) in the form

$$\delta Y = A*\delta OPAQ + B*\delta PR0 + C*\delta PR1 + D*\delta PR2 + E*\delta PR3 + F*\delta PR4 + G*\delta PR5 \qquad (15)$$

Multiple regression shows no memory of cloud for previous months. Since we are using anomalies, the leading coefficient is of order zero, so it is not shown. After standardization, all variables are dimensionless.

4.1 Memory of cold season precipitation in April climatology

On the Prairies precipitation memory lasts through winter, as water is stored until the snowpack melts in late March or April. The reflective snow cover on the Prairies, with an albedo ≈ 0.7, acts as a climate switch that reduces T_m by 10°C (Figures 2 and 5). April is the month when the snowpack finally melts and the ground thaws. Table 2a shows selected April standardized anomalies regressed on standardized anomalies of opaque cloud for April; and precipitation from April back to November (coefficients A to G in equation (15)). We see that the April monthly anomalies show memory of the anomalies of precipitation back 5 months through the entire cold season to November, when typically the ground begins to freeze, and the first lasting snow occurs (Figure 5). Some of this memory remains in the March snowpack depth (not shown here, see [16]).

For the first row, δOPAQ-Apr, the large negative coefficients for the monthly anomalies δDTR, δT_x and δP_{LCLx}, mean that these variables decrease with increasing opaque cloud cover; while the positive sign for the δRH_n and δRH_m means they increase with opaque cloud. For δT_x and δDTR (and δT_m, not shown), the negative coefficients, B to G, for the months March back to November, mean that the positive cold season precipitation anomalies are correlated with cold April temperatures. For δRH_n, δRH_m (and δRH_x not shown), the positive coefficients, B to G, mean that positive cold season precipitation anomalies are correlated with higher RH in April. Most coefficients for δDTR, δRH_n, δRH_m and δP_{LCLx} (representative of afternoon cloud-base) have a 99% confidence ($p<0.01$).

There are several physical processes that are probably involved. The precipitation over the cold season is mostly stored in the snowpack till spring, when melt absorbs energy and cools the surface; and the melt also provides water for evaporation, which also cools and increases RH. In addition the freeze-up of the soil in November may similarly preserve November precipitation anomalies as soil ice through the cold season till spring melt.

In April the high albedo of the remaining snowpack, as well as fresh snow, also play a direct climate role, as discussed in section 3.4 and shown in Figure 2, because snow cover acts as a climate switch. So we computed the standardized April snow cover frequency anomaly, from the fraction of days in April with snow depth >0, and added this to the multiple regression (15) to give

$$\delta\text{Y-Apr} = \text{A}^*\,\delta\text{OPAQ}_m\text{-Apr} + \text{B}^*\delta\text{PR-Apr} + \text{C}^*\delta\text{PR-Mar} + \text{D}^*\delta\text{PR-Feb} + \text{E}^*\delta\text{PR-Jan} + \text{F}^*\delta\text{PR-Dec} + \text{G}^*\delta\text{PR-Nov} + \text{T}^*\delta\text{SnowCover-Apr} \quad (16)$$

Table 2b shows the coefficients from equation (16). There is an increase in R^2 for all variables, and especially for T_x in comparison with Table 2a. For maximum temperature, T_x, snow cover frequency anomalies have as large an impact as opaque cloud anomalies. Note that the coefficients G for δPR-Nov for δRH_n, δRH_m and δP_{LCLx} are not significant, but the coefficients G for δDTR and δT_x have a confidence > 99% in both Table 2a and 2b. It is possible that this is the cooling impact in April coming from the melt of soil-ice frozen back in November.

Table 2. Standardized regression coefficients for April anomalies in anomalies δDTR, δT_x, δRH_n, δRH_m and δP_{LCLx} on standardized anomalies of a) opaque cloud and precipitation; b) Adding fraction of April days with snow cover. For coefficients: boldface represents $p<0.01$ (>99%); roman represents $0.01 \le p < 0.05$, and coefficients are omitted for $p > 0.05$.

a) Variable	**δDTR**	**δT_x**	**δRH_n**	**δRH_m**	**δP_{LCLx}**
620 months R^2	**0.67**	**0.47**	**0.65**	**0.63**	**0.66**
$\delta OPAQ_m$-Apr (A)	**-0.52±0.02**	**-0.78±0.04**	**0.76±0.03**	**0.60±0.03**	**-0.93±0.04**
δPR-Apr (B)	**-0.06±0.02**		**0.20±0.03**	**0.17±0.03**	**-0.19±0.04**
δPR-Mar (C)	**-0.12±0.02**	**-0.22±0.04**	**0.23±0.03**	**0.19±0.02**	**-0.27±0.03**
δPR-Feb (D)	**-0.07±0.02**	**-0.12±0.04**	**0.16±0.03**	**0.13±0.02**	**-0.19±0.03**
δPR-Jan (E)	**-0.09±0.02**	**-0.19±0.04**	**0.17±0.03**	**0.13±0.02**	**-0.21±0.03**
δPR-Dec (F)	**-0.06±0.02**		**0.16±0.03**	**0.14±0.02**	**-0.19±0.03**
δPR-Nov (G)	**-0.08±0.02**	**-0.13±0.04**	0.07±0.03	**0.08±0.02**	**-0.11±0.03**
b) Variable	**δDTR**	**δT_x**	**δRH_n**	**δRH_m**	**δP_{LCLx}**
550 months R^2	**0.73**	**0.65**	**0.80**	**0.70**	**0.78**
$\delta OPAQ_m$-Apr (A)	**-0.49±0.02**	**-0.57±0.04**	**0.65±0.03**	**0.54±0.03**	**-0.82±0.04**
δPR-Apr (B)	-0.04±0.02		**0.16±0.03**	**0.15±0.03**	**-0.15±0.04**
δPR-Mar (C)	**-0.08±0.02**	-0.07±0.03	**0.14±0.03**	**0.14±0.03**	**-0.18±0.03**
δPR-Feb (D)	**-0.05±0.02**		**0.09±0.03**	**0.10±0.03**	**-0.11±0.03**
δPR-Jan (E)	**-0.05±0.02**		0.06±0.03	**0.07±0.03**	**-0.08±0.03**
δPR-Dec (F)	**-0.04±0.02**		**0.12±0.02**	**0.13±0.02**	**-0.16±0.03**
δPR-Nov (G)	**-0.06±0.02**	**-0.10±0.03**			
δSnowCover-Apr (T)	**-0.19±0.02**	**-0.63±0.04**	**0.52±0.03**	**0.31±0.03**	**-0.57±0.03**

Peer-reviewed version available at Environments 2018, 5, 129; doi:10.3390/environments5120129

Table 2 shows that the climate in April, when the snow pack finally melts, has memory of precipitation back through the entire winter to November. Most of the variability in the April climate is explained by anomalies of winter precipitation and the fraction of days in April with residual snow cover.

4.2 Growing season memory of precipitation

After snowmelt on the Prairies, the transition into the growing season months May to August (MJJA) is rapid, and typically the memory of precipitation for the months May to August goes back only to March or April [16]. Merging the 2466 MJJA growing season months gives a unified description for the growing season correlation of the thermodynamic anomalies with opaque cloud and lagged precipitation, shown in Table 3, adapted from [16]. We retain precipitation anomalies for 4 months.

Table 3. Standardized multiple regression coefficients for the MJJA growing season merge of 2466 months. For coefficients: boldface represents p<0.01 (>99%); roman represents 0.01≤p<0.05, and coefficients are omitted for p>0.05.

Variable	A ($\delta OPAQ_m$)	B ($\delta PR0$)	C ($\delta PR1$)	D ($\delta PR2$)	E ($\delta PR3$)	R^2
δT_x	**-0.95±0.02**	**-0.07±0.02**	**-0.16±0.02**			0.58
δT_m	**-0.67±0.02**	**0.03±0.02**	**-0.10±0.02**			0.43
δT_n	**-0.34±0.02**	**0.18±0.02**		0.04±0.02		0.13
δDTR	**-0.61±0.01**	**-0.26±0.01**	**-0.15±0.01**	**-0.05±0.01**	**-0.03±0.01**	0.73
δRH_n	**0.59±0.01**	**0.37±0.01**	**0.23±0.01**	**0.09±0.01**	**0.03±0.01**	0.69
δRH_m	**0.53±0.01**	**0.32±0.01**	**0.24±0.01**	**0.11±0.01**	**0.04±0.01**	0.61
δRH_x	**0.38±0.02**	**0.20±0.02**	**0.20±0.01**	**0.10±0.01**	0.04±0.01	0.36
δDRH	**-0.22±0.01**	**-0.18±0.01**	**-0.03±0.01**			0.26
δP_{LCLx}	**-0.76±0.02**	**-0.42±0.02**	**-0.31±0.01**	**-0.13±0.01**	**-0.05±0.01**	0.68
δP_{LCLm}	**-0.55±0.01**	**-0.30±0.01**	**-0.25±0.01**	**-0.12±0.01**	**-0.04±0.01**	0.62
δP_{LCLn}	**-0.30±0.01**	**-0.15±0.01**	**-0.16±0.01**	**-0.08±0.01**	**-0.03±0.01**	0.36
δDP_{LCL}	**-0.46±0.01**	**-0.27±0.01**	**-0.15±0.01**	**-0.05±0.01**		0.58
$\delta \theta_{Ex}$	**-0.55±0.02**	**0.28±0.02**	**0.08±0.02**	**0.12±0.02**		0.21
$\delta \theta_{Em}$	**-0.42±0.02**	**0.30±0.02**	**0.09±0.02**	**0.11±0.02**		0.17
$\delta \theta_{En}$	**-0.22±0.02**	**0.34±0.02**	**0.09±0.02**	**0.11±0.02**		0.13
$\delta D\theta_E$	**-0.32±0.01**	**-0.06±0.01**				0.37
δQ_m	**-0.06±0.02**	**0.41±0.02**	**0.22±0.02**	**0.16±0.02**		0.22

Peer-reviewed version available at *Environments* **2018**, *5*, 129; doi:10.3390/environments5120129

Table 3 shows that only some anomalies, such as δDTR, δRH_n, δRH_m, δP_{LCLx} with high R^2 values, are correlated with precipitation anomalies going back three months. As in Table 2, the OPAQ coefficients A are typically the largest, except notably for δQ_m.

The first groups are the regression coefficients for the temperature anomalies, δT_x, δT_m, δT_n, and δDTR, which were all standardized by the SD of δT_m. The fit represented by R^2 is largest for DTR, and decreases from δT_x to δT_n. All the temperature variable anomalies show a strong inverse correlation with opaque cloud anomalies that reflect the downward SW radiation. The warm season is dominated by negative SWCF as shown in Figure 3. The negative values of A decrease from δT_x to δT_n. δDTR has a negative correlation to both cloud anomalies, and to precipitation anomalies going back for 3 months. Note that because all the temperatures were standardized by the SD of δT_m, the coefficients for the diurnal range are the difference of the corresponding coefficients for the maximum and minimum. For example, A(δDTR) = -0.61 = A(δT_x) – A(δT_n). Further, B(δDTR) = -0.26 = B(δT_x) – B(δT_n) (rounded to 2 significant figures) shows the role of the positive correlation of T_n with precipitation anomalies for the current month. We see that the coefficients B change sign in the sequence from δT_x to δT_m to δT_n. This means that although T_m falls strongly with cloud, its coupling to precipitation is weak because the coefficients B and C have opposite sign, in contrast to the RH anomalies discussed below. This regression analysis clearly shows that mean temperature anomalies, δT_m, are strongly coupled to cloud, and therefore solar forcing, but rather weakly to precipitation; while δDTR (and δT_x) decrease with both cloud and precipitation. We cannot infer causality from multiple regressions, but negative B for δT_x is consistent with evaporation from moist soils reducing T_x, and the positive B for δT_n is consistent with the fact that under wetter conditions the fall of T_n at night is limited by saturation.

The next group are the four RH anomalies, δRH_x, δRH_m, δRH_n, and δDRH. For the first three, the regression coefficients show that positive RH anomalies are correlated with positive cloud and precipitation anomalies; and the coefficients are significant for both present and three past months. The coefficients for δDRH are negative because δRH_n increases faster with cloud and precipitation than δRH_x; and the coefficients are significant for only one past month. The R^2 fit decreases monotonically from the afternoon minimum δRH_n to δRH_m to the sunrise maximum δRH_x to δDRH. The diurnal cycle of T and RH have an inverse dependence on opaque cloud, reaching T_x and RH_n in the afternoon at the same time [16]. This is related to the fact that mixing ratio Q is tightly constrained by BL transports, which we will discuss in section 4.3. But over land, near-surface RH is constrained by the availability of soil moisture for evaporation from bare soil and transpiration (which is often modeled as a stomatal resistance to evaporation [22, 23]. Soil moisture anomalies are related in turn to precipitation anomalies. We see that afternoon RH_n and mean RH_m anomalies have a strong positive correlation to precipitation anomalies, and a large R^2. However, RH_x, which increases with precipitation, is limited if surface saturation is reached and dew forms before sunrise. Because the latent heat release slows the temperature fall, it is consistent that RH_x and T_n anomalies are both positively coupled to wetter precipitation anomalies for the current month (coefficient B).

The third group in Table 3 is the four P_{LCL} anomalies: P_{LCLx} is generally representative of afternoon cloud-base [9]. P_{LCL} has a strong dependence on RH and a weak dependence on T, and we see that negative P_{LCL} anomalies are coupled to positive cloud and precipitation anomalies. The coefficients are largest for afternoon δP_{LCLx}, for which R^2 is high. The coefficients for δP_{LCLx}, δP_{LCLm}, δP_{LCLn} are all 99% significant for both present and three past months, showing that cloud-base anomalies have a long memory of precipitation anomalies in the growing season.

The fourth group in Table 3 shows the coefficients for $\delta\theta_{Ex}$, $\delta\theta_{Em}$, $\delta\theta_{En}$ and $\delta D\theta_E$. The first three show the decrease with increased cloud, but an increase with precipitation. The R^2 values are small, even though the coefficients have 99% confidence. The diurnal range of θ_E is dominated by the dependence of DTR on opaque cloud. The two afternoon anomalies, $\delta\theta_{Ex}$ and δP_{LCLx}, are related to moist convective instability, which is favored by higher θ_{Ex} and lower cloud base.

The diurnal variation of mixing ratio, Q, has a double maxima and minima, which we will show in section 4.3, so Table 3 shows only the coefficients for mean anomaly δQ_m. The R^2 fit is much smaller for Q than for RH. The negative correlation to opaque cloud is small because T and RH have an inverse diurnal dependence on cloud. The positive correlation to precipitation anomalies goes back 2 months, consistent with positive precipitation anomalies increasing evapotranspiration.

Table 3 summarizes the multiple regression correlation coefficients between warm season near-surface variables and opaque cloud and lagged precipitation, and gives a quantitatively useful target for the evaluation of the coupled processes in models. Two important conceptual results emerge for the monthly mean climate on the Canadian Prairies. Afternoon anomalies of δT_x, δRH_n, δP_{LCLx} are strongly correlated to opaque cloud anomalies. Correlation with precipitation anomalies are weaker, but stretch back for three past months for these key variables. Anomalies of Q_m are coupled to precipitation anomalies with memory of two months past, but have weak correlation to opaque cloud.

4.3 Growing season coupling of the diurnal cycle to precipitation and cloud

Figure 6 showed the very tight coupling in the warm season between opaque cloud and the diurnal range of key thermodynamic variables on daily timescales. Table 3 used multiple linear regression to show the correlation of the monthly anomalies of thermodynamic variables to anomalies of opaque cloud and precipitation. Table 3 confirms the strong correlation with opaque cloud, but shows that the coefficients for the lagged precipitation anomalies differ considerably for different variables.

For a graphical representation [16] we approximate by defining a weighted precipitation anomaly δPRwt, based on precipitation for just the current and the past month

$$\delta PRwt = 0.6^* \,\delta PR0 + 0.4^* \,\delta PR1 \tag{17}$$

This simplification, with this choice of coefficients in the ratio of 1.5, captures much of the precipitation dependence for the variables that have the highest R^2, such as DTR, RH_n, and P_{LCLx}, because these have the ratio of the coefficients B/C ≈ 1.5 in Table 3.

The x-axis of Figure 7 is 0.1 bins of $OPAQ_m = \delta OPAQ_m + 0.46$, where 0.46 is the mean opaque cloud over all the months. For each MJJA month (total 2466 months) we computed the weighted anomaly δPRwt from (17), and added the MJJA mean precipitation rate of 1.8 mm d^{-1} to give PRwt = δPRwt + 1.8. We then stratified the data into three ranges of PRwt of <1.2 mm d^{-1}; 1.2 to 2 mm d^{-1} and >2 mm d^{-1}, which have mean values of 0.9, 1.6 and 2.6 mm d^{-1}. There are (531, 1103, 832) months in these three PRwt bins. To generate Figure 7, we compute for each variable bin, the mean and standard error (SE) of the anomalies, and add back the MJJA variable means.

Figure 7 (top-left) shows DTR and its components, T_x and T_n, top-right shows DRH, RH_x and RH_n, bottom-left shows $D\theta_E$, θ_{Ex} and θ_{En} and bottom-right is DP_{LCL}, P_{LCLx} and P_{LCLn}. The strong dependence on opaque cloud, seen in Figure 6, clearly dominates most of these climate variables, since T falls and RH increases with increasing cloud. This is turn is connected to the weak dependence of Q on cloud (Table 3). The color scheme is red and blue respectively for the dry and wet precipitation bins. As PRwt falls, DTR increases faster than T_x.

Figure 7 (top-right) shows that RH_x and RH_n (and RH_m, not shown) increase with both cloud and PRwt, but because afternoon RH_n increases faster than RH_x, DRH decreases with increasing PRwt. Note the rise of RH_x with PRwt towards saturation. If RH_x reaches saturation at the surface on individual days, condensation of dew and the release of latent heat limit the fall of T_n.

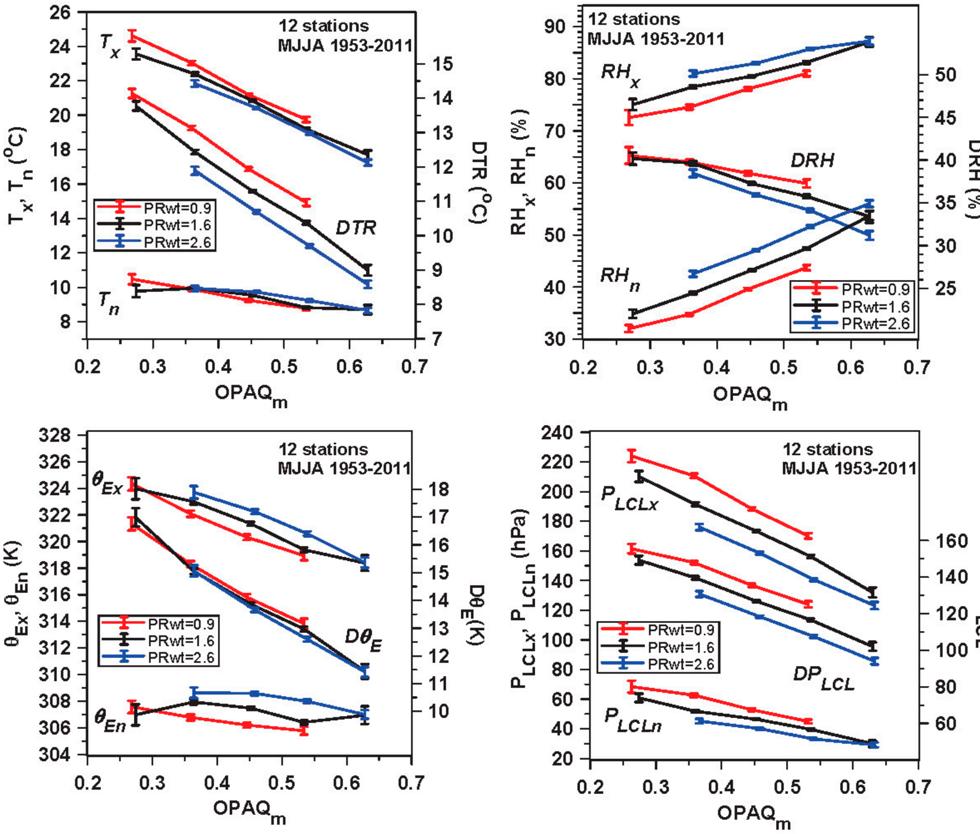

Figure 7. Coupling between DTR, T_x and T_n (top-left), (top-right) DRH, RH_x and RH_n, (bottom-left) $D\theta_E$, θ_{Ex} and θ_{En} and (bottom-right) DP_{LCL}, P_{LCLx} and P_{LCLn} and opaque cloud fraction and weighted precipitation in mm d^{-1}.

Figure 7 (bottom panels) show the variables that determine the BL coupling to clouds and precipitation. Afternoon P_{LCLx} and θ_{Ex} determine the cloud-base height and moist adiabat. Both θ_{Ex} and θ_{En} increase with PRwt, but the diurnal range $D\theta_E$ depends primarily on cloud not precipitation, as shown in Table 3. All the P_{LCL} variables decrease with increasing PRwt. The sunrise minimum of P_{LCLn} falls with PRwt, as the surface moves towards saturation. So higher precipitation, which we can loosely associate with increased daytime evapotranspiration, ET, corresponds with a lower monthly mean cloud base and higher θ_E in the afternoon, which would both favor increased convective instability.

In the warm season on the Prairies, the diurnal cycle of mixing ratio Q has two maxima and minima except under cloudy conditions [9, 14, 16]. We can graph this dependence on anomalies of opaque cloud cover, $\delta OPAQ_m$, and weighted precipitation anomalies, $\delta PRwt$ from equation (17) in mm d^{-1}, from the MJJA growing season merge of 2466 months.

Peer-reviewed version available at *Environments* **2018**, *5*, 129; doi:10.3390/environments5120129

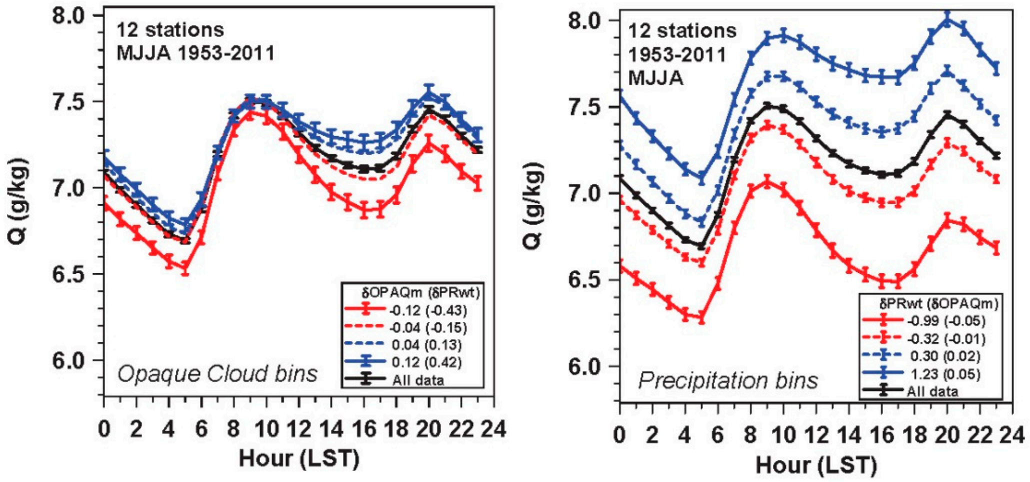

Figure 8. Dependence of diurnal cycle of Q on opaque cloud bins (left) and weighted precipitation bins (right).

Figure 8 (left panel) shows the stratification by δOPAQ$_m$ into four ranges: δOPAQ$_m$ < -0.08; -0.08 to 0; 0 to 0.08 and >0.08, based on the SD of δOPAQ$_m$ ≈ 0.08. There are (371, 839, 909, 347) months in these respective bins. We averaged in bins the diurnal cycle of the anomalies from the station monthly means, calculate the SE, and add back the 12-station MJJA mean of Q. The legend shows the mean value for each δOPAQ$_m$ bin, and in parentheses the corresponding mean of δPRwt. As mean δOPAQ$_m$ increases from -0.12 to +0.12, mean δPRwt increases from – 0.43 to +0.42 mm d^{-1}. We have binned by δOPAQ$_m$ but mean OPAQm and precipitation increase together (Figure 6). The small increase in Q$_m$ with δOPAQ$_m$ is consistent with Table 3.

The sunrise minimum of Q occurs at the minimum temperature, when the night-time BL is shallow with a strong temperature inversion. As the surface net radiation turns positive after sunrise, it drives increasing surface sensible and latent heat fluxes. This warms and moistens a shallow ML trapped beneath the stable nocturnal inversion, and there is a steep rise of Q. When the surface potential temperature reaches that of the top of the capping inversion in mid-morning, the ML deepens more rapidly, typically mixing into a deep drier residual ML from the previous day, so that Q falls to the afternoon minimum. With less cloud and more solar forcing, the ML can grow deeper, and mix with more dry air from above, so both the morning rise and mid-day fall of Q are larger in Figure 8. Finally Q rises again to an evening maximum as the surface layer cools and uncouples from the deep BL, while ET continues.

Figure 8 (right panel) is the corresponding partition into four ranges of weighted precipitation anomalies: δPRwt < -0.7; -0.7 to 0; 0 to 0.7 and >0.7 mm d^{-1}, based on the SD of δPRwt ≈ 0.7 mm d^{-1}. There are (387, 961, 745, 373) months in these respective bins. The legend shows the mean value for each δPRwt bin, and again in parentheses the corresponding mean of δOPAQ$_m$. With increasing δPRwt, there is a large upward shift of the mean diurnal cycle of Q, as Q$_m$ increases with precipitation anomalies, which we can associate with increased soil moisture and ET. As mean δPRwt increases from – 0.99 to +1.23 mm d^{-1}, mean δOPAQ$_m$ increases from -0.05 to +0.05, and the fall of Q from mid-morning maximum to afternoon minimum is reduced as in the left panel.

Clearly we are dealing with a fully coupled system, but Figure 3 shows that climatologically, while the amplitude of the diurnal cycle of Q increases a little with reduced cloud cover (presumably increased solar forcing and vertical mixing), there is a large upward shift in the diurnal cycle with increased weighted precipitation, presumably from increased ET.

Peer-reviewed version available at Environments 2018, 5, 129; doi:10.3390/environments5120129

5. Seasonal climate issues

5.1 Seasonal extraction of surface total water storage

We made a simplified estimate of the growing season water and energy budgets of the Prairies in [12], using fits between opaque cloud and cloud forcing (see section 3.3) to estimate the surface radiation budget. We calculated the seasonal change in total water storage from the GRACE, using the gridded 1x1 degree monthly land mass grids [7,8], version JPL-RL05.DSTvSCS1401, for liquid water equivalent thickness for the decade 2002-2012. This allowed us to link the draw-down of total water storage (TWS) [24, 25] to precipitation anomalies during the growing season. We will present a brief overview, referring to [12] for discussion of some of the uncertainties.

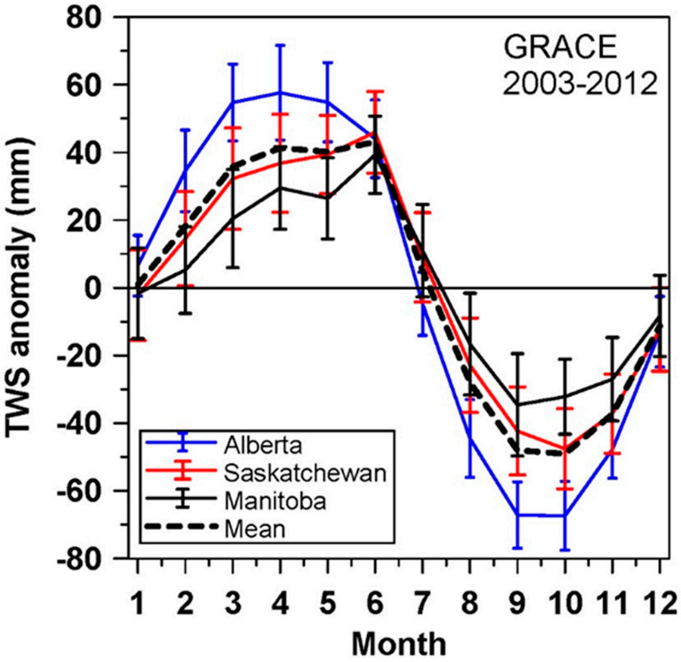

Figure 9. Mean annual cycle of GRACE TWS anomaly by province.

Figure 9 shows mean annual cycle of the monthly anomalies of TWS from the annual mean, with the small 2002-2012 trend removed. Although the data have been interpolated to a 1x1 degree grid for user convenience, the effective spatial resolution of the GRACE data is about 300 km, so we averaged over the Prairie regions of the three provinces. The amplitude of the mean annual cycle is 90mm. We computed ΔTWS:MJJA, the growing season drawdown of TWS for MJJA, as the difference between August 31 (mean of August and September) and May 1 (mean of April and May) for each year and province. Mean drawdown is ΔTWS:MJJA = -79mm.

We regressed the anomalies of ΔTWS:MJJA for the 2002-2012 onto the corresponding anomalies of MJJA precipitation, derived from the monthly archive (http://ec.gc.ca/dccha-ahccd/) of the second generation adjusted precipitation dataset [26]. The linear regression fit [12] with R^2 =0.56, is

$$\Delta\text{TWS:MJJA} = -0.59(\pm 0.08) + 0.56(\pm 0.09)\ \delta\text{Precip(MJJA)} \tag{18}$$

The mean value of Precip(MJJA) for 2002-2012 (details in [12]) is 2.32 mm d^{-1}, while the mean drawdown of TWS is 0.59 mm d^{-1} for δPrecip(MJJA) = 0; or 25% of the mean precipitation. Thus equation (18) shows that, as δPrecip(MJJA) decreases from +1 to -1 mm d^{-1}, ΔTWS:MJJA increases from near zero to -1.15 mm d^{-1}, which corresponds to -141mm over the 123 day growing season. The coupling coefficient of 0.56(±0.09) in equation (18) is effectively a 56±9% damping coefficient for precipitation anomalies in the growing season by changes in the drawdown of TWS. This drawdown of stored water in the growing season means that ET > precipitation, and this difference increases in dry summers.

5.2 Impact of land-use change on growing season climate

In the past thirty years there has been a major change in land use across the Canadian Prairies, specifically the conversion of more than five million hectares of summer fallow to continuous cropping. The large increase in the area of cropland has increased summer transpiration, which has reduced maximum temperatures in the growing season over the Prairies [27]. Other analyses of US Midwest summer temperature maxima also show a cooling from land-use change to cropland [28] and cropland intensification [29].

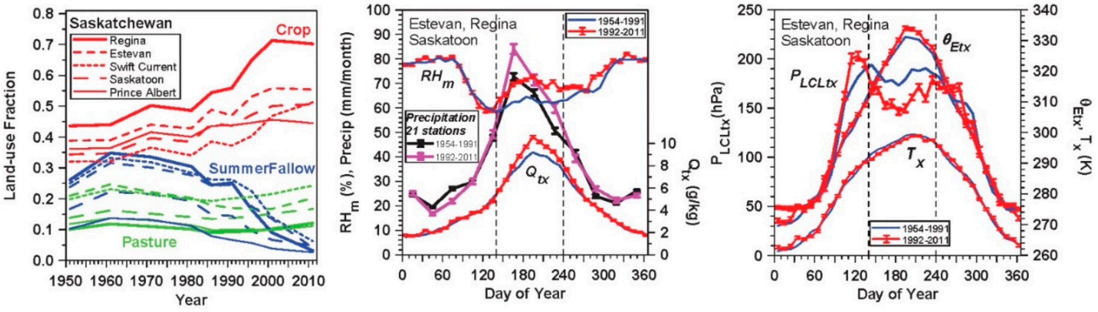

Figure 10. Long term trends in total cropland, pasture, and summer fallow around five climate stations in Saskatchewan (left); (center) RH_m, Q_{tx} and mean precipitation in southern Saskatchewan, and (right) mean changes in annual cycle of T_x, P_{LCLtx} and θ_{Etx} for Saskatoon, Regina and Estevan.

Figure 10 summarizes the long-term climate impact of the reduction of summer fallow in Saskatchewan [10, 15]. The left panel shows the land-use trends in total cropland, pasture, and summer fallow around five climate stations in Saskatchewan. The 50km radius circles around each station in Figure 1 were used to generate local averages of the ecodistrict crop data [10]. We split the climate station time-series into two periods: a longer historic period, 1954-1991, when summer fallow cover was large (although slowly decreasing) and a recent 20-year period, 1992-2011, when summer fallow has fallen rapidly to its present low value [30]. We did not attempt any analysis of decadal trends.

Saskatoon, Regina and Estevan in Saskatchewan have complete datasets and show similar changes between the two time periods, so we averaged them as 10-day means [10]. The center panel shows the mean changes in precipitation, RH_m, and mixing ratio Q_{tx} at the time of the afternoon T_x. We show the standard errors (SE) of the difference between the two mean time series as an indication of significance. For precipitation, which has much more variability than temperature and humidity, we used monthly precipitation for the 21 stations in Saskatchewan south of 53.22°N, from the second generation adjusted precipitation dataset [26]. Error bars are the SE of each monthly mean. The right panel shows the corresponding changes in the annual cycle of T_x, P_{LCLtx} and θ_{Etx} between the two time periods.

It is clear that there are significant changes in the growing season climate between the historic period, 1953-1991, and the more recent period since 1992. The vertical dashed lines mark the period $140 \le DOY < 240$ (May 20-August 27) considered in [10] to be representative of the crop growing season. Over this time window, the growing season is cooler since 1992, with a drop of T_x of -0.93±0.09 K, and significantly moister with a rise of (RH_m, Q_{tx}) of (6.9±0.2%, 0.70±0.04 gkg^{-1}). There is a corresponding fall of the P_{LCLx} of 22.3±1.1 hPa, and a small rise of θ_{Etx} of 1.1±0.2 K, both at the time of afternoon T_x. There is also an increase of summer (June, July and August) precipitation of 25.9±4.6 mm.

It is reasonable to conclude that we are seeing the fully coupled response to the large shift from summer fallow to intensive cropping. It seems that more intensive agriculture has increased transpiration, which has cooled and moistened the growing season climate, lowering cloud-base and increasing equivalent potential temperature. The coupled increase of Q with precipitation is consistent with Figure 8; and the increase of summer precipitation is consistent with the increase in moist instability represented by lower afternoon P_{LCLx} and higher θ_{Etx}. Not shown here is a distribution shift in cloud frequency: with 6% fewer days with 2-4 tenths and 7% more with 7-10 tenths cloud cover [10].

5.3 Warm season atmospheric and surface energy budgets

The Prairie climate data have no surface nor TOA fluxes, so we will use flux data from ERA-Interim to put our analyses in the context of the atmospheric and surface energy budgets for the MJJA warm season. We used gridpoint data co-located with the four climate stations Estevan, Regina, Saskatoon and Prince Albert in Saskatchewan that were used in [31] to analyze the near-surface biases of temperature in ERA-Interim. We computed the terms in the atmospheric TOA and surface energy budget, first on a daily basis, and then for each MJJA station-year, dropping a few days in May with surface snow cover. Figure 11 is a simplified graphical representation of the key flux terms for this region of the central Prairies from 49.2 to 53.2°N.

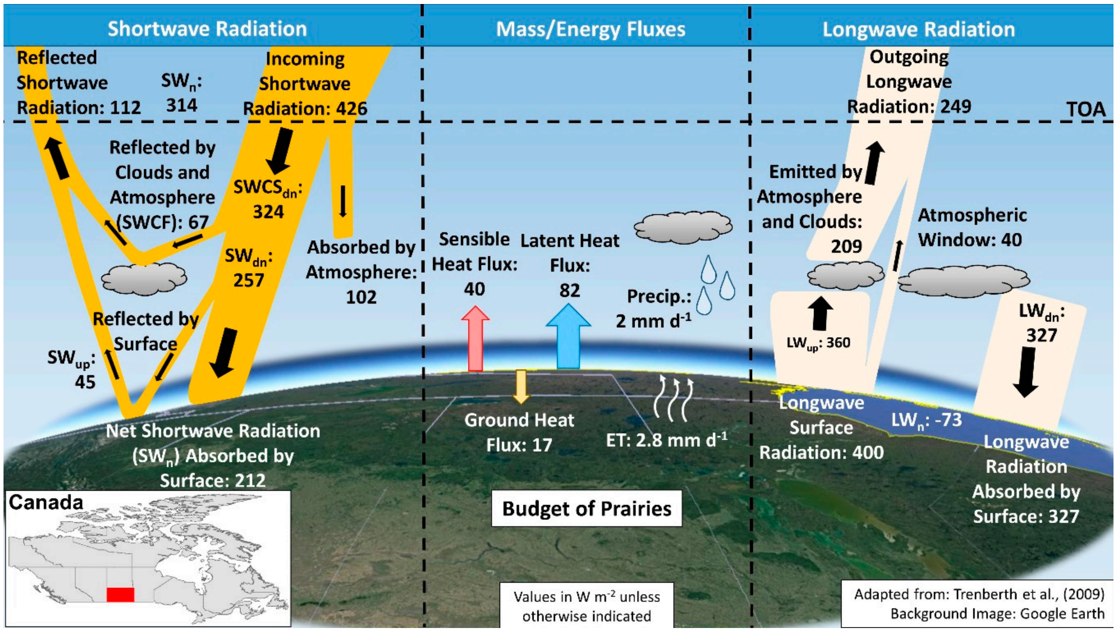

Figure 11. Schematic for surface and TOA energy budgets for Prairie region of southern Saskatchewan.

On the left is the SW budget terms. Part of the incoming TOA solar flux is absorbed by the atmosphere, part reflected by clouds and atmospheric aerosols, and part is reflected by the surface; so that surface SW_n = 212 W m^{-2} is about half the TOA downward flux. On the right is the LW budget terms, where the upward surface LW emission of 400 W m^{-2} is mostly absorbed by the atmospheric greenhouse gases, primarily water vapor and CO_2, as well as by clouds. About 10% escapes to space through the atmospheric infrared window. Clouds and atmosphere re-emit to space, and back to the surface, giving a surface LW_n = -73 Wm^{-2}. The resulting surface R_n = 139 W m^{-2} balances the upward sensible and latent heat fluxes (40 and 82 W m^{-2} respectively) and the growing season warming of the ground of 17 W m^{-2}, which is probably too large [31]. For the MJJA surface water budget, precipitation is 2 mm d^{-1} and evapotranspiration, ET is 2.8 mm d^{-1}. ET exceeds precipitation in the growing season, because of the substantial drawdown of surface water storage discussed in section 5.1. The TOA SW_n > outgoing LW for the MJJA warm season.

Table 4 stratifies the 140 station years of data into ECA bins, showing how reflective cloud cover changes the TOA and surface energy budgets. The mean values across all the data are the data lines in red, which have been shown rounded in Figure 11. The model sign convention is downward fluxes

Peer-reviewed version available at *Environments* **2018**, *5*, 129; doi:10.3390/environments5120129

are positive and upward fluxes are negative. The number of station-years in each bin, denoted by K, is not uniform, nor is the distribution across the four stations. Nonetheless, there is a uniform progression as reflective cloud (ECA) increases: TOA SW$_n$, surface SW$_{dn}$, net radiation, R$_n$, the sensible heat flux, SH, Bowen ratio, BR, and the 2-m temperatures all decrease, while the latent heat flux, LH, and precipitation increase. There is compensation between the surface SW$_n$ and LW$_n$ fluxes as reflective cloud changes, which reduces the change in R$_n$. If there is less reflection by clouds, SW$_{dn}$ increases, and this warms the surface and LW$_{up}$ increases. Because the decrease of cloud cover and precipitation are coupled, and ET changes much less than precipitation, we see that the surface BR increases by a factor of two as cloud cover and precipitation decrease.

The reanalysis is a fully coupled model representation of the Prairie climate for this 35-y period, mapped here in terms of changing ECA. On average ET exceeds precipitation by 0.86 mm d^{-1}, which is largely consistent with the budget analysis in section 5.1 based on the GRACE data. There is a substantial MJJA drawdown of about 80 mm of soil water (not shown), because the model has four soil layers to a total depth of 2.89 m with a dynamic range of water storage of 150 mm per meter between field capacity and permanent wilting point. However, the model soil water budget has additional increments, because the soil moisture reanalysis uses observed 2-m values of temperature and humidity and satellite estimates of soil moisture [32] to minimize the model 2-m temperature forecast errors. Despite this analysis correction, we found in [31] that on daily timescales, ERA-Interim in the warm season has a cold bias in T$_x$ and a warm bias in T$_n$, so that DTR is biased low; and these biases increase under clear skies. Table 4 stratifies four-month composites by ECA, so it is not directly comparable to the daily analysis in [31], but it is likely that T$_x$ and T$_n$ in Table 2 have respectively cold and warm biases of about 1°C.

Table 4. Surface and TOA fluxes for the MJJA warm season from ERA-Interim for 1979-2013, stratified by ECA, derived from the gridpoints for Estevan, Regina, Saskatoon and Prince Albert, SK.

ECA	K	TOA SW$_{dn}$	TOA SW$_n$	Surf SWCS$_{dn}$	Surf SW$_{dn}$	SWCF	Surf SW$_{up}$	Surf SW$_n$	Surf Albedo	TOA LW$_{up}$	Surf LWup	Surf LW$_{dn}$	Surf LW$_n$
0.146	11	427	326	327	279	-48	-54	225	0.19	-257	-412	328	-84
0.178	34	427	320	325	268	-58	-49	218	0.18	-252	-406	329	-77
0.203	47	426	315	324	258	-66	-45	213	0.17	-250	-400	327	-74
0.230	32	424	310	322	248	-74	-40	208	0.16	-247	-396	326	-69
0.278	16	427	299	323	233	-90	-38	195	0.16	-242	-389	325	-64
0.207	**140**	**426**	**314**	**324**	**257**	**-67**	**-45**	**212**	**0.17**	**-249**	**-400**	**327**	**-73**

ECA	K	R$_n$	SH	LH	BR	G	PRECIP	ET	Runoff	T$_x$	T$_m$	T$_n$	DTR
0.146	11	141.6	-53.2	-71.8	0.78	16.7	1.13	-2.48	0.07	24.4	18.5	12.1	12.3
0.178	34	141.4	-46.1	-77.4	0.62	17.9	1.69	-2.67	0.04	23.0	17.4	11.2	11.8
0.203	47	139.6	-41.1	-81.5	0.53	17.0	1.91	-2.82	0.06	22.0	16.5	10.5	11.5
0.230	32	138.3	-33.3	-88.9	0.39	16.1	2.18	-3.07	0.13	21.0	15.8	10.1	11.0
0.278	16	130.8	-30.9	-84.5	0.37	15.4	2.92	-2.92	0.13	19.4	14.5	9.2	10.3
0.207	**140**	**138.9**	**-40.3**	**-81.8**	**0.52**	**16.8**	**1.97**	**-2.83**	**0.08**	**21.9**	**16.5**	**10.6**	**11.4**

6. Conclusions

We have reviewed progress in the quantitative understanding of the coupling between the land surface, clouds, precipitation, snow cover and the climate system that came from analysis of the long-term hourly Canadian Prairie dataset. This progress was possible because, along with conventional hourly measurements, trained observers recorded opaque cloud fraction hourly across the Prairies for the past 60 years. These 24 daily estimates of opaque cloud are of sufficiently quality that they can be calibrated against BSRN data to give the climatology of the daily short-wave, longwave and total cloud forcing. This key radiative forcing of the surface energy budget has previously not been available for long-term climate datasets. We found that net cloud radiative forcing reverses sign from negative in the warm season to positive in the cold season with snow cover. This transforms the coupling between cloud cover and the diurnal cycle between warm and cold seasons in the warm season, maximum temperature increases with decreasing opaque cloud, while minimum temperature barely changes; while in the cold season with snow cover, maximum temperature decreases with decreasing cloud and minimum temperature decreases even more. Although our results are stratified by the observed opaque cloud cover, we show the regression equations (10) and (11) that convert opaque cloud into cloud radiative forcing.

We showed the many ways in which snow cover acts as a climate switch between two non-overlapping climate regimes, producing a systematic cooling of 10°C or more. With fresh snow cover in November, temperature falls 10°C during the transition. Simply separating cold season days into those with and without snow cover shows these are two distinct climates, again separated by 10°C. The traditional merging of these two climates is unrepresentative, since typically the near-surface boundary layer also changes from unstable to stable with snow cover. As cloud cover falls, the climate cooling with snow increases. Mean cold season temperatures fall almost 1.5°C for each 10% increase in the fraction of days with snow cover.

In the warm season with no snow cover, the diurnal ranges of temperature, relative humidity, equivalent potential temperature and the pressure height of the lifting condensation level all fall steeply with increasing opaque cloud cover. Remarkably this tight coupling between diurnal range and cloud cover is almost unchanged from April to September, so we provide quadratic fits to the mean profiles. Given 600 station-years of hourly data, we are able to extract, perhaps for the first time, the relationship between cloud forcing and the warm season imbalance of the diurnal cycle. This imbalance over 24 h changes monotonically from a +2°C warming and a -6% drying under clear skies to a -1.5°C cooling and 6% moistening under cloudy skies with precipitation. Correspondingly there is a 24h rise of θ_E and LCL under clear skies and a fall of both under cloudy skies (see section 3.5).

On daily timescales the radiative forcing dominates, and the changing cloud forcing drives the changing diurnal cycle of the thermodynamic variables. On longer timescales, monthly and seasonal, precipitation anomalies, stored as soil moisture anomalies, change ET and modify the diurnal response. Because we have the large daily cloud radiative forcing, we can show statistically that the memory of water storage anomalies, from precipitation and the snowpack, goes back many months. The spring climatology for April shows the memory of snowfall back through the entire winter, and the memory in summer months goes back to the months of snowmelt.

In addition, we showed how the thermodynamic coupling of the diurnal cycle to the cloud forcing is modified by lagged precipitation anomalies. With reduced precipitation, the diurnal ranges of T, RH and P_{LCL}, but not θ_E, increase. With increased precipitation, afternoon T_x falls a little, while RH_n and θ_{Ex} increase and P_{LCLx}, representing cloud-base, falls.

Climatologically, the diurnal cycle of Q has a sunrise minimum, a rise to a mid-morning maximum while evaporation is trapped beneath the nocturnal inversion, then a fall to an afternoon minimum, as water vapor is rapidly transported upward into a deep daytime BL; followed by a second rise to an evening minimum as the surface cools and starts to uncouple from the mixed BL. We showed that while the amplitude of the diurnal cycle of Q increases a little with reduced cloud cover (presumably from increased solar forcing and vertical mixing), there is a large upward shift in the diurnal cycle of Q as weighted precipitation increases, presumably from increased evaporation.

The GRACE satellite data from a recent period show that the seasonal extraction of the surface total water storage is a large damping of the interannual variability of precipitation anomalies in the growing season. Over a range of precipitation anomalies of ±1mm d^{-1}, seasonal extraction of ground water increases from near-zero with high precipitation to 1.15 mm d^{-1} for low precipitation.

Also on seasonal timescales, the large land-use change on the Prairies from summer fallowing to intensive cropping, with the most rapid transition in the early 1990s, has led to a coupled climate response that has cooled and moistened the growing season, lowering cloud-base, increasing equivalent potential temperature, and increasing precipitation.

Finally we compute the atmospheric energy and water budgets for four stations in Saskatchewan for the 35-y period of the ERA-Interim reanalysis to show graphically the mean TOA and surface budgets representative of the Canadian Prairies for the MJJA growing season. We also show the dependence of these budgets on reflective cloud cover for this fully coupled model system.

More broadly, these long-term climate datasets from the Prairies can be used to improve the representation of clouds and land-surface processes in numerical forecast models. A preliminary step was the assessment of the biases in the surface diurnal cycle of temperature in ERA-Interim [31], but much more is possible. For example, knowledge of the biases is providing meteorological information for regions where no data were previously available. We plan to investigate the impact of these biases on model estimates of crop yields and greenhouse gas emission estimates using the DNDC model [33]. With the improved knowledge of the energy budget for the Prairies, we can now investigate which management practices could significantly change the energy budget and allow farmers opportunities to minimize their impact on climate change.

Supplementary Materials: The Canadian Prairie data are available from the first author, or from Environment and Climate Change Canada at http://climate.weather.gc.ca/. The reanalysis data are available from ECMWF at https://ecmwf.int/en/research/climate-reanalysis/era-interim.

Author Contributions: Conceptualization, writing—original draft preparation, AB.; writing—review and editing, AB and RD.

Funding: This research was partially supported by Agriculture and Agri-Food Canada, contract number 3000662193, with technical support from ECMWF.

Acknowledgements: We are very grateful to the Canadian station observers who have made hourly climate observations for many decades.

Conflicts of Interest: The authors declare no conflict of interest.

References

1. Betts, A. K. Understanding Hydrometeorology using global models. *Bull. Amer. Meteorol. Soc.* **2004**, *85*, 1673-1688.
2. Betts, A. K. Land-surface-atmosphere coupling in observations and models. *J. Adv. Model. Earth Syst.* **2009**, *1*, Art. #4, 18 pp., doi: 10.3894/JAMES.2009.1.4
3. Betts, A. K; Viterbo, P. Land-surface, boundary layer and cloud-field coupling over the south-western Amazon in ERA-40. *J. Geophys. Res.* **2005**, *110*, D14108, doi:10.1029/2004JD005702.
4. Koster, R. D.; Schubert, S. D.; Suarez, M. J. Analyzing the Concurrence of Meteorological Droughts and Warm Periods, with Implications for the Determination of Evaporative Regime. *J. Climate* **2009**, *22*, 3331–3341.
5. Leung, R. L.; Qian, Y.; Bian, X. Hydroclimate of the western United States based on observations and regional climate simulation of 1981–2000. Part I: Seasonal Statistics. *J. Climate* **2003**, *16*, 1892–1911.
6. Berg, A.; Lintner, B. R.; Findell, K.; Seneviratne, S. I.; van den Hurk, B.; Ducharne, A.. Chéruy, F.; Hagemann, S.; Lawrence, D. M.; Malyshev, S.; Meier, A.; Gentine, P. Interannual coupling between summertime surface temperature and precipitation over land: Processes and implications for climate change. *J. Climate* **2015**, *28*, 1308–1328.
7. Swenson, S. C.; Wahr, J. Post-processing removal of correlated errors in GRACE data, *Geophys. Res. Lett.* **2006**, *33*, L08402, doi:10.1029/2005GL025285.
8. Landerer, F.W.; Swenson, S. C. Accuracy of scaled GRACE terrestrial water storage estimates. *Water Resources Research* **2012**, *48*, W04531, 11 pp, doi:10.1029/2011WR011453.
9. Betts, A.K.; Desjardins, R.; Worth, D. Cloud radiative forcing of the diurnal cycle climate of the Canadian Prairies. *J. Geophys. Res. Atmos.* **2013**, *118*, 8935–8953, doi:10.1002/jgrd.50593.
10. Betts, A.K.; Desjardins, R.; Worth, D.; Cerkowniak, D. Impact of land use change on the diurnal cycle climate of the Canadian Prairies, *J. Geophys. Res. Atmos.* **2013**, *118*, 11,996–12,011, doi:10.1002/2013JD020717.
11. Betts, A.K.; Desjardins, R.; Worth, D.; Wang, S.; Li, J. Coupling of winter climate transitions to snow and clouds over the Prairies. *J. Geophys. Res. Atmos.* **2014**, *119*, 1118-1139, doi:10.1002/2013JD021168.

12. Betts, A.K.; Desjardins, R.; Worth, D.; Beckage, B. Climate coupling between temperature, humidity, precipitation and cloud cover over the Canadian Prairies. *J. Geophys. Res. Atmos.* **2014**, *119*, 13305-13326, doi:10.1002/2014JD022511.
13. Betts, A.K.; Desjardins, R.; Beljaars, A.C.M.; Tawfik, A. Observational study of land-surface-cloud-atmosphere coupling on daily timescales. *Front. Earth Sci.* **2015**, *3:13*. http://dx.doi.org/10.3389/feart.2015.00013
14. Betts, A.K.; Tawfik, A.B. Annual Climatology of the Diurnal Cycle on the Canadian Prairies. *Front. Earth Sci.* **2016**, *4:1*, 1-23. doi: 10.3389/feart.2016.00001.
15. Betts, A.K.; Desjardins, R.; Worth, D. The Impact of Clouds, Land use and Snow Cover on Climate in the Canadian Prairies. *Adv. Sci. Res.* **2016**, *13*, 37-42, doi:10.5194/asr-13-37-2016
16. Betts, A.K.; Tawfik, A.B.; Desjardins, R.L. Revisiting Hydrometeorology using cloud and climate observations. *J. Hydrometeor.* **2017**, *18*, 939-955, http://dx.doi.org/10.1175/JHM-D-16-0203.1
17. Zeng, X.; Wang, A. What is monthly mean land surface air temperature? *Eos Trans.* **2012**, *93 (15)*, p156, doi: 10.1029/2012EO150006.
18. Wang, A.; Zeng, X. Range of monthly mean hourly land surface air temperature diurnal cycle over high northern latitudes, *J. Geophys. Res. Atmos.* **2014**, *119*, 5836–5844, doi:10.1002/2014JD021602.
19. Li, Z.; Wang, K.; Zhou, C.; Wang, L. Modelling the true monthly mean temperature from continuous measurements over global land. *Int. J. Climatol.* **2016**, *36*: 2103–2110, doi: 10.1002/joc.4445.
20. Dee, D. P.; Uppala, S. M.; Simmons, A. J.; Berrisford, P.; Poli, P.; Kobayashi, S.; Andrae, U.; Balmaseda, M.A.; Balsamo, G.; Bauer, P.; et al. The ERA-Interim reanalysis: configuration and performance of the data assimilation system. *Quart. J. Roy. Meteorol. Soc.* **2011**, *137*, 553 - 597. DOI: 10.1002/qj.828.
21. Betts, A. K.; Chiu, J. C. Idealized model for changes in equilibrium temperature, mixed layer depth and boundary layer cloud over land in a doubled CO2 climate. *J. Geophys. Res.* **2010**, *115*, D19108, 2009JD012888.
22. Monteith, J. L. Climate and the efficiency of crop production in Britain, Philos. Trans. R. Soc. London 1977, Ser. B, 281, 277–294.
23. Collatz, G. J.; Ball, J. T.; Grivet, C.; Berry, J. A. Physiological and environmental regulation of stomatal conductance, photosynthesis, and transpiration: A model that includes a laminar boundary layer. *Agric. For. Meteorol.* **1991**, *54*, 107– 136.
24. Yang, Z.-L.; Niu, G.-Y.; Mitchell, K. E. ; Chen, F. ; Ek, M. B.; Barlage, M. ; Longuevergne, L. ; Manning, K. ; Niyogi, D. ; Tewari, M. ; Xia, Y. The community Noah land surface model with multiparameterization options (Noah-MP): 2. Evaluation over global river basins. *J. Geophys. Res.* **2011**, *116*, D12110, doi:10.1029/2010JD015140.
25. Cai, X.; Yang, Z.-L. ; David, C. H.; Niu, G.-Y.; Rodell, M. Hydrological evaluation of the Noah-MP land surface model for the Mississippi River Basin. *J. Geophys. Res. Atmos.* **2014**, *119*, 23–38, doi:10.1002/2013JD020792.
26. Mekis, É.; Vincent, L.A.; An overview of the second generation adjusted daily precipitation dataset for trend analysis in Canada. *Atmosphere-Ocean* **2011**, *49(2)*, 163-177.
27. Gameda, S.; Qian, B.; Campbell, C.A. ; Desjardins, R.L. Climatic trends associated with summerfallow in the Canadian Prairies. *Agric. Forest Meteorol.* **2007**, *142*, 170–185. doi:10.1016/j.agrformet.2006.03.026.
28. Bonan, G. D. Observational evidence for reduction of daily maximum temperature by croplands in the Midwest United States, *J. Climate* **2001**, *14*, 2430-2442.
29. Mueller, N. D.; Butler, E. E.; McKinnon, K. A.; Rhines, A.; Tingley, M.; Holbrook, N. M.; Huybers, P. Cooling of US Midwest summer temperature extremes from cropland intensification, *Nature Climate Change* **2016**, *6*, 317-322, doi:10.1038/nclimate2825.
30. Dumanski, J.; Desjardins, R. L.; Tarnocai, C.; Monreal, C. ; Gregorich, E. G. ; Kirkwood, V. ; and Campbell, C. A. Possibilities for future carbon sequestration in Canadian agriculture in relation to land use changes. *Climatic Change* **1998**, *40*, 81-103.
31. Betts, A.K.; Beljaars A.C.M. Analysis of near-surface biases in ERA-Interim over the Canadian Prairies. *J. Adv. Model. Earth Syst.* **2017**, *9*, doi:10.1002/2017MS001025.
32. Wagner, W.; Hahn, S.; Kidd, R.; Melzer, T.; Bartalis, Z.; Hasenauer, S.; Figa-Saldaña, J.; de Rosnay, P.; Jann, A.; Schneider, S.; et al. The ASCAT Soil Moisture Product: A Review of its Specifications, Validation Results, and Emerging Applications. *Meteorologische Zeitschrift* **2013**, *22, No. 1*, 1–29. DOI: 10.1127/0941-2948/2013/0399.

Peer-reviewed version available at *Environments* **2018**, *5*, 129; doi:10.3390/environments5120129

33. Smith, W.N., Grant, B.B.; Desjardins, R.L.; Worth, D.; Li, C.; Boles, S.H.; Huffman, E,C.. A tool to link agricultural activity data with the DNDC model to estimate GHG emission factors in Canada. *Agriculture, Ecosystems and Environment* **2010,** *136 (3-4)*, 301-309.